# 7
# Microstructured Reactors for Fluid–Fluid Reactions

In this chapter, fluid–fluid flow patterns and mass transfer in microstructured devices are discussed. The first part is a brief discussion of conventional fluid–fluid reactors with their advantages and disadvantages. Further, the classification of fluid–fluid microstructured reactors is presented. In order to obtain generic understanding of hydrodynamics, mass transfer, and chemical reaction, dimensionless parameters and design criteria are proposed. The conventional mass transfer models such as penetration and film theory as well as empirical correlations are then discussed. Finally, literature data on mass transfer efficiency at different flow regimes and proposed empirical correlations as well as important hydrodynamic design parameters are presented.

## 7.1
## Conventional Equipment for Fluid–Fluid Systems

Fluid–fluid systems are widely used in chemical, petroleum, pharmaceutical, hydrometallurgical, and food industries. Commercially important examples of gas–liquid mass transfer with or without reaction include gas purification, oxidation, halogenations, hydrogenation, and hydroformylation to name but a few. Important liquid–liquid reactions include nitration, phase transfer catalysis (PTC), cyclization, emulsion polymerization, homogenous catalyst screening, enzymatic reactions, extraction, precipitation, crystallization, and cell separation.

Conventionally, a wide variety of equipment is used for fluid–fluid applications involving gas–liquid and liquid–liquid systems: stirred tanks, bubble columns, centrifugal-, packed-, plate columns, Buss loop reactors, straight or coiled tubular reactors, static mixer reactors, and film reactors. The schematics of these equipments are depicted in Figure 7.1. The contacting principles are bubbling, filming, spraying of one fluid into the other or disturbing the two-phase flow stream to create turbulence. The conventional equipments work well for most slow and moderately fast reactions. However, for fast intrinsic kinetics the overall transformation rate is controlled by mass transfer.

*Microstructured Devices for Chemical Processing,* First Edition.
Madhvanand N. Kashid, Albert Renken and Lioubov Kiwi-Minsker.

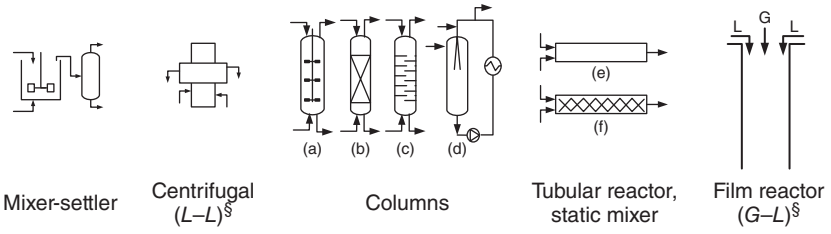


**Figure 7.1** Conventional equipment used for fluid–fluid reactions (columns: (a) multistage agitated column, (b) packed column, (c) sieve tray column, (d) buss loop reactor, (e) tubular reactor, and (f) static mixer) § *G* – Gas, *L* – liquid. (Adapted with permission from Ref. [1]. Copyright (2009) American Chemical Society.)

The advantages and limitations of fluid–fluid reactors are listed in Table 7.1. Stirred tanks are the most commonly used for reactions involving fluid–fluid systems. Bubble columns are used for gas–liquid reactions, while centrifugal reactors are used for liquid–liquid systems with low density differences. The third variety of equipment, the columns, is commonly used in chemical industries in their countercurrent mode of operations. Tubular contactors offer a number of advantages because of their flexibility, simplicity, and wide range of operating windows. To intensify the mixing in the tubular reactor, internals like static mixers are useful. Such equipment is used for mixing immiscible liquids in a compact configuration and is found to be effective [2].

In falling film contactors, a thin film is created by a liquid falling under gravity pull. The liquid flows over a solid support, which is normally a thin wall or stack of pipes. In conventional falling film devices, a film with a thickness of 0.5–3 mm is generated [3]. The film flow becomes unstable at high throughput and the film may break up into rivulets, fingers, or a series of droplets at high flow rates.

A common drawback of all the above mentioned equipments is the inability to condition the drop or film size precisely and to avoid the nonuniformities that arise because of the complex hydrodynamics. This leads to uncertainties in the design and often imposes severe limitations on the optimal performance.

Multiphase microstructured devices can potentially be used to diminish the limitations of conventional reactors. They generally take advantage of their large interfacial area reducing the mass transfer resistances.

## 7.2
## Microstructured Devices for Fluid–Fluid Systems

Microstructured devices for fluid–fluid systems exist in a number of configurations. They can be roughly classified into three types based on the contacting principles [1]: micromixer, microchannels, and falling film microreactors. The first two types of devices are used for all fluid–fluid applications while the microstructured falling film reactor is used only for gas–liquid systems. Depending on the application, these microstructured devices can also be used in series, for example,

**Table 7.1** Different types of fluid–fluid reactors, their advantages, and limitations.

| Reactors | Advantages | Limitations |
|---|---|---|
| Stirred tank | Low maintenance cost | Difficult to condition the drop/bubble size |
| | Intense mixing gives higher performance | Difficult to separate small density difference fluids |
| Bubble column | Simple construction | Very complex hydrodynamics |
| | Mixing because of sparged gas – requires low energy | Applicable only for slow reactions |
| Centrifugal contactor | Works at low density differences between two fluids | Difficult to scale up |
| | Less solvent volume required for extraction | Mechanical complexity and high maintenance cost |
| | Rapid mixing and separation can enhance product recovery and cost | |
| Static mixers | Easy to operate | Performance completely dependent on packing/internals |
| | Satisfactory performance at lower cost | Good performance only in a limited range of flow rates |
| Loop reactor | Better temperature control | Difficult to handle rapid fouling materials |
| | Higher productivity | High probability of residence time distribution in the loop |
| Tubular reactor | Behavior close to plug flow | Not suitable for slow reactions |
| | High heat and mass transfer rates – suitable for highly exothermic/endothermic reactions | Difficult to use high viscous fluids |
| Falling film | Low pressure drop | Unstable at high throughput |
| | High interfacial area | Thick liquid film results in higher mass transfer resistance for three-phase reactions |

the first mixer for creating dispersion and second mixer for allowing the transport and/or chemical transformation.

### 7.2.1 Micromixers

These are the devices in which fine dispersion occur because of high flow rates or static internals. Three types of mixers are available: mixer-settler [4, 5], cyclone [6], and interdigital mixer [3] (see Figure 7.2). The principle of fluid contacting in micromixer-settler is almost similar to the conventional mixer-settler assembly. However, because of the reduced size of the equipment, the moving part of the mixer is replaced by the static. Two-fluid streams are introduced from the top of mixer and biphasic mixture is taken out from the top central line, which is further introduced to the mini-settler where the phases disengage based on their density

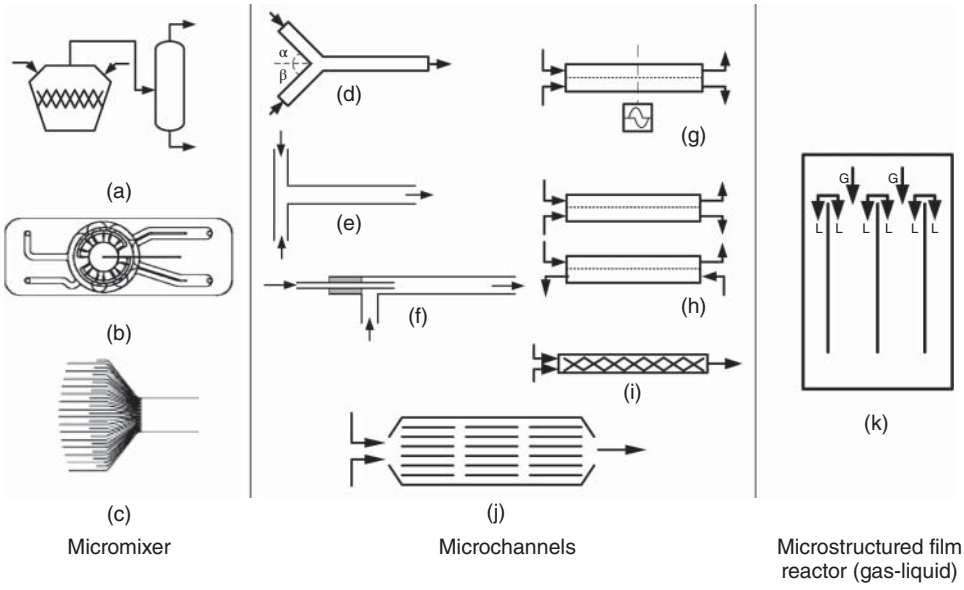


**Figure 7.2** Schematic representation of fluid–fluid microstructured reactors: (a) micromixer settler, (b) cyclone mixer, (c) interdigital mixer, microchannels with (d) inlet Y, (e) T-shaped inlet, (f) concentric inlet, (g) microchannel with partial overlap, (h) microchannel with membrane or metal contactor, (i) microchannel with static internals bed, (j) parallel microchannels with internal redispersion units, (k) microstructured falling film reactor. (Adapted with permission from Ref. [1]. Copyright (2009) American Chemical Society.)

difference [4]. The advantage of mixer-settler over channel reactors is that drop size and specific interfacial area can be changed over a wide range in a given reactor. While there is an increase in the inlet flow velocity, the drop size decreases and thus specific interfacial area increases. The maximum values of specific interfacial area are reached within less than 1 s, being up to fivefold higher than other microstructured reactors [5]. It is also possible to use arrays of multiple static elements in the mixer to extend the throughput. However, similar to conventional contactor it is difficult to control the bubble/drop sizes precisely and thus the interfacial area.

In the cyclone mixer (Figure 7.2b), two phases are dosed through two different nozzles. The bubble size can be influenced by the arrangement of gas and liquid injection nozzles (either parallel or vertical) [6]. The spiral patterns of the gas bubbles similar to cyclone vortex are formed in the liquid. Another type of mixer – interdigital mixer (Figure 7.2c) – induces the immiscible fluid streams to merge with or without prior splitting of the different phases into finer substreams. The reaction channel downstream of the mixing section is of sufficiently large diameter so that the small bubbles generated in the mixing section flow in the form of foam or emulsion [3].

### 7.2.2 Microchannels

Microchannels use mainly Y-shaped, T-shaped or concentric contacting geometry (Figure 7.2d–f), for a two-phase contact, which further flows through a channel with or without structured internals. These microchannels can be divided into various types such as microchannels with partial overlapping (Figure 7.2g), microchannels with mesh contactors (Figure 7.2h) (porous membrane, sieve-like structure, etc.), microchannels with static mixer (Figure 7.2i), and multichannel contactors with intermediate redispersion units (Figure 7.2j).

#### 7.2.2.1 Microchannels with Inlet T, Y, and Concentric Contactor

In this case the contacting of two fluids is restricted to uniting only the fluid streams using Y, T- types of junctions, or concentric inlets. These contactors are used as a laboratory tool for the application requiring precise definition of flow regime and specific interfacial area for mass transfer. Depending on the flow mixer geometry, physical properties of fluids, and operating conditions, different flow regimes are observed. The flow regime and mass transfer performance of such single channel reactors are discussed in detail in the next section.

#### 7.2.2.2 Microchannels with Partial Two-Fluid Contact

In this type of channel, anodically bonded silicon/glass plates, each carrying a single channel with rectangular and semicircular cross section, are fitted in order to form partially overlapping channels (see Figure 7.2g). The advantage of this microstructured reactor (MSR) is that the contact between two fluids can be adjusted depending on the application. Partially overlapping channels MSR were developed for liquid–liquid extraction by Central Research Laboratory (CRL), UK [7]. The concept was tested for large throughput and 120 identical contactors were operated in parallel in one device [8]. Out of this work a platform for the use of microstructured contactor for liquid–liquid extraction was created.

#### 7.2.2.3 Microchannels with Mesh or Sieve-Like Interfacial Support Contactors

Similarly to partially overlapping channels, microchannels with mesh contactors (Figure 7.2h) are used to create the partial contact of fluids. The advantage of these contactors is that both modes of operation, cocurrent and countercurrent, can be applied. Besides, the flow is stabilized because of the solid support between two fluids. The solid contactors are porous membrane [9, 10] and metal sheets with sieve-like structure [11]. Similarly to parallel flow, the mass transfer in both cases is only by diffusion and the flow is under laminar flow regime dominated by capillary forces. The membrane contactor has the advantage of being flexible with respect to the ratio of two fluids. In addition to flow velocities, the mass transfer is a function of membrane porosity and thickness. In another type of microextractor, two microchannels are separated by a sieve-like wall architecture to achieve the separation of two continuous phases. However, the hydrodynamics in both types of contactors is more complex because of interfacial support and bursting of fluid

from one channel to the other at higher pressure drop in case countercurrent flow limits their applications.

#### 7.2.2.4 Microchannels with Static Mixers

In this case, contacting of two fluids is achieved either by uniting, dividing and recombining fluid streams or using static internals in the microchannels (Figure 7.2i). A large number of small reaction volumes can be handled serially in a flow channel known as *digitalization* [12]. Different T-shaped and Y-shaped contactors can be used to split the flow stream into two equal flow streams of biphasic mixture and change the size of the drops. In addition, by changing the diameter of the channel and creating resistance to the flow, multiple drops can be united and the interfacial area can be decreased.

An example for microchannels with structured internals are caterpillar micromixer, where the surfaces consist of ramp-like structures, moving the fluid constantly up and down and the fluid contact is achieved by a sequence of repeated splitting-reshaping-recombination processes [5]. Sometimes simple foam stacks are used as static mixer for dispersing two immiscible phases.

#### 7.2.2.5 Parallel Microchannels with Internal Redispersion Units

In this case, the redispersion units are placed along the length of the parallel microchannels and are made of a metal sheet having multiple channels Figure 7.2j or with metal foam. The aim is to provide continuously large surface area by repetitive formation and breaking of the drops [13].

### 7.2.3 Microstructured Falling Film Reactor for Gas–Liquid Reactions

The falling film MSR is one of the most commonly used devices for gas–liquid reactions (examples are given in gas–liquid reactions section). The liquid flows downward because of gravity in the form of film and gas flows through the open space that lies in the top cover of the housing. The falling film contactor consists in general of a stainless steel plate with open channels, typically 300 μm deep, separated by about 100 μm thick walls. The role of open microchannels is to prevent the breakup of the liquid film.

Because of capillary force and small channels' width, surface wetting liquids are pulled along the walls, thus forming a flowing meniscus. With increasing flow rate, the thickness of the film increases and its surface becomes flatter.

The specific gas–liquid interfacial area can attain up to 20 000 $m^2\ m^{-3}$, which is 2–3 orders of magnitude larger than conventional bubble columns and agitated vessels (200 $m^2\ m^{-3}$).

The main drawback of the microstructured falling film reactor is the short residence time of the liquid in the channels, which typically varies between 5 and 20 s, depending on physical properties of the liquid and the operating conditions. The residence time can be increased by lengthening the microchannel or by decreasing the angle of descent, which can be achieved by helicoidal microchannel falling

film reactor. The residence time could be increased by a factor of about 50 in a microchannel with an angle of descent decreased from 90° to 7.5° [14].

## 7.3 Flow Patterns in Fluid–Fluid Systems

### 7.3.1 Gas–Liquid Flow Patterns

Depending on reactor geometry and operating conditions, different flow regimes such as bubbly flow, Taylor flow, slug bubbly flow, slug annular, churn flow, and annular flow are observed in microstructured reactors [15–17]. On the basis of the forces acting on the gas–liquid flows, these flow regimes can be classified as surface tension dominated and transition and inertia dominated as shown in Figure 7.3.

The main problem for controlling the flow pattern is its dependence on many experimental parameters such as flow velocity, flow ratio of phases, fluid properties, channel geometry, microchannel material, wall roughness, pressure, and temperature. All these parameters influence the relative importance of the different forces. Different flow regimes in gas–liquid flows in microstructured reactors are discussed in the following section.

#### 7.3.1.1 Bubbly Flow

Bubbly flow in microstructured reactors occurs in different types of geometries as shown in Figure 7.4. It is characterized by the bubbles with diameters less than or equal to the capillary diameter. In a microchannel, this flow pattern typically occurs at relatively high liquid velocities and low gas velocities [16]. For a given set of operating conditions, the gas inlet channel of the two fluids mixing element decides the bubble size. This limitation is circumvented by flow focusing geometries that consist of a gas-feeding nozzle positioned upstream of an orifice (50–200 μm) through which a liquid stream is forced [18, 19]. For a gas dispersion smaller than 20%, the bubble size is as small as 10 μm and is always smaller than the orifice (ratio of bubble size to orifice $\approx 0.1-0.6$).

The gas dispersion is further increased using multilamination mixer in which both gas and liquid inlet channels are increased and fed into one outlet channel [22, 23]. If the maldistribution is avoided in inlet channel and geometry is optimized, a bubble size of 30–50 μm with a variation of 10% can be obtained. The flow behavior varies from plug flow to partially backmixed flow depending on the width of the channel and flow velocity. Backmixing increases with increased total flow rate and gas–liquid ratio and is affected by the reactor tube orientation with vertical tubes showing up to five times higher backmixing compared to the horizontal tube [24].

The bubbly flow in a single channel at low gas hold-up (Figure 7.4a) shows well-defined specific interfacial area, which is, however, a way below to other flow regimes. At high gas hold-up, the small size of the bubble provides very high

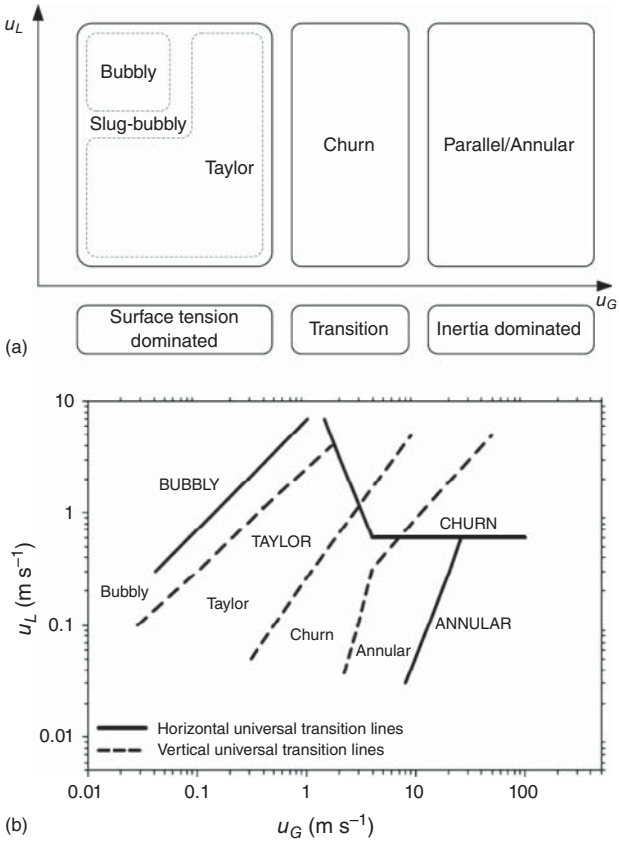


**Figure 7.3** Classification of flow patterns. (a) General classification and (b) comparison of flow pattern transition lines in horizontal and vertical channels – a universal map for gas–liquid systems ($d_h = 0.1–1$ mm) [17]. Regimes in capital are for horizontal flow map, while regimes in lower case are for vertical flow map. (Adapted with permission from Elsevier.)

specific interfacial area (Figure 7.4b–d). However, nonuniform drop size, flow instability, backmixing, and difficulties in the characterization of performance parameters limit its use.

#### 7.3.1.2 Taylor Flow

This flow regime is the most commonly observed in microchannels and is also referred to as *slug and train flow*. As mentioned before, the bubble size is restricted by channel dimensions. With smaller channels and relatively low liquid velocity, elongated cylindrical bubbles longer than the channel diameter are formed because of pressure squeezing mechanism in the surface tension dominated region. In some cases this flow is further introduced in a wider channel, referred to as *delay tube*, to form bubbly flow with higher gas hold-up of up to 90% as shown in Figure 7.4b–d [20].

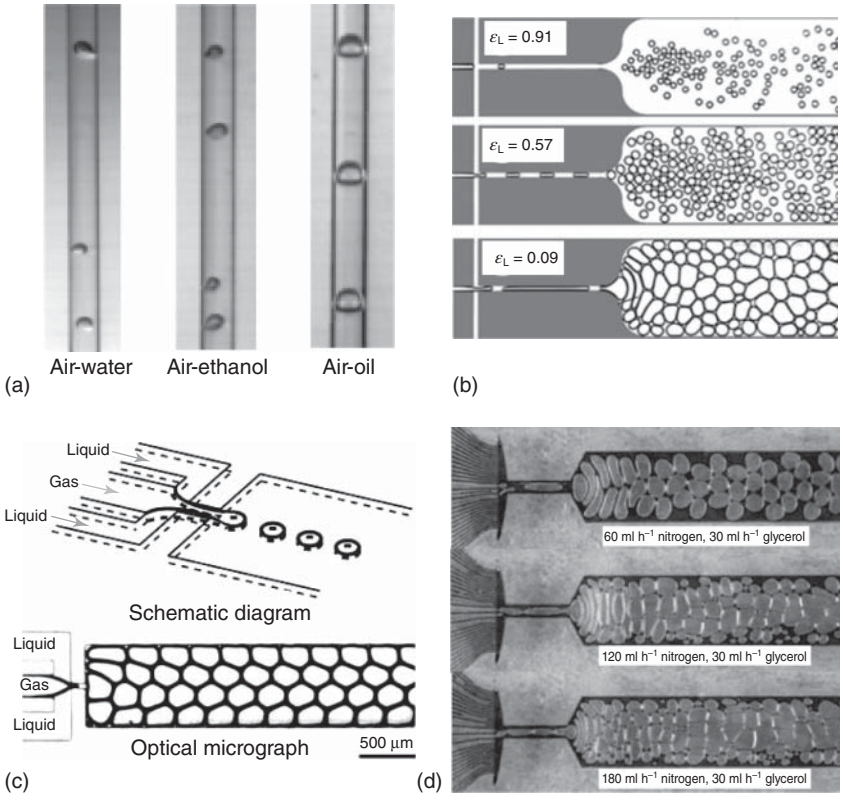


**Figure 7.4** Bubbly flow in different types of devices. (a) Vertical glass capillary. (Adapted with permission from Ref. [16]. Copyright (2005) American Chemical Society.) (b) Cross flow mixing element for foam flow generation. (Adapted from Ref. [20].) (c) Flow focusing device [21]. (Adapted with permission from Nature Publishing Group.) (d) Foam formation in slit-shaped glass mixer [22]. (Adapted with permission from Elsevier.)

Five steps of Taylor flow generation, adapted from liquid–liquid systems [25], are briefed (Figure 7.5):

(i) Initially the dispersed phase penetrates the main stream and the bubble begins to grow.
(ii) As the tip of the dispersed phase grows, it blocks almost the whole cross section of the main channel, which in turn builds pressure upstream. The radius of the tip curvature is limited by the dimensions of the channel. The continuous phase flows in the gap between the wall and the dispersed phase drop with higher flow velocity.
(iii) Because of the shear exerted by the continuous fluid and the pressure drop along the channel length, the bubble elongates and grows downstream. The interface approaches the downstream inlet of the dispersed phase and a slug is formed in the main channel.

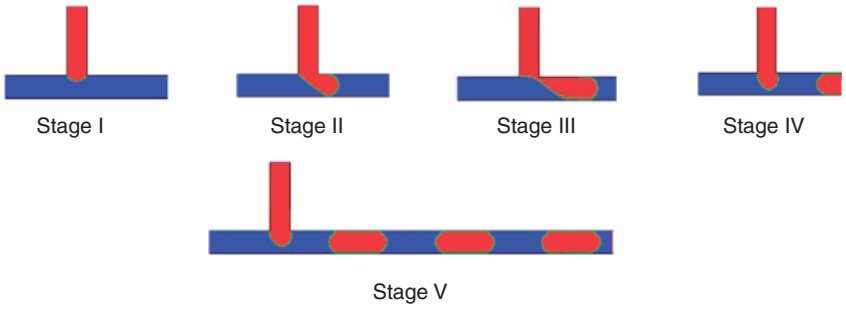


**Figure 7.5** Five steps of Taylor (slug) flow generation. Dispersed gas phase is introduced through side channel while wetting continuous phase is introduced through main channel.

(iv) The neck of the immiscible liquid gets squeezed further, that is, the radial curvature dominates the axial and the slug separates from the dispersed phase stream.
(v) The processes of bubble penetration and separation from the dispersed phase continue and produce a well-defined slug flow.

Depending on flow rates and fluid properties, the bubbles often have hemispherical shaped tops and flattened tails [16].

The wide applications of Taylor flow for reactions and separations come from its stability and ability to provide well-defined high specific interfacial area. The recirculation within the liquid slugs improves heat and mass transfer from liquid to wall and interfacial mass transfer from gas to liquid [26]. It reduces axial dispersion and enhances radial mixing. The radial mixing can further be enhanced using meandering channels as shown in Figure 7.6c [27].

In Taylor flow, liquid phase forms a thin wall film providing lubricating action to the enclosed bubbles and, as a consequence, bubbles flow at relatively higher velocity than the liquid. The interfacial gas–liquid area thus comprises two parts: the lateral part (that of the wall film) and the perpendicular part (between the bubble and the adjacent liquid slug). Often the length of the bubble is many times greater than the channel diameter resulting in higher contribution of lateral part than the perpendicular part.

The thickness of the wall film in Taylor flow in capillaries is mainly dependent on the ratio of viscous to interfacial forces, which is given by the capillary number, *Ca*.

$$Ca_i = \frac{\mu_i \cdot u_b}{\sigma}; \text{with } u_b, \text{the bubble velocity} \tag{7.1}$$

*Ca* is mostly referred to the continuous phase ($i = C$); this corresponds to the liquid phase ($i = L$) in gas–liquid systems.

Different correlations can be found in the literature for estimating the thickness of the wall film. The majority of the studies suggest that the film thickness ($\delta_{\text{film}}$) is a function of capillary diameter ($d_t$) and capillary number ($Ca$). Two correlations, Bretherton [28] and Aussillous and Quere [29], are widely used.

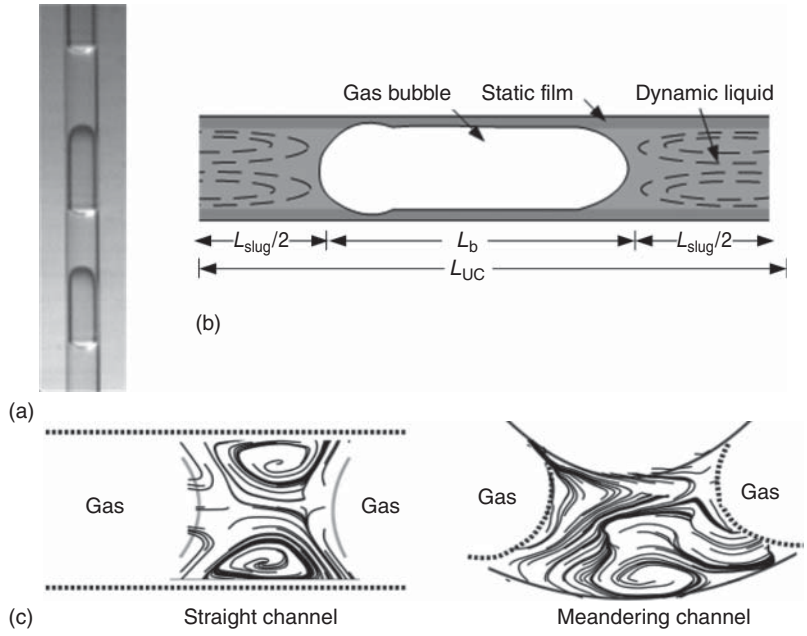


**Figure 7.6** Experimental snapshots and schematic presentation of Taylor flow in different configurations. (a) Taylor flow in vertical capillary. (b) Schematic presentation of Taylor flow in horizontal capillary ($L_b$ – length of bubble and $L_{UC}$ – unit slug length). (Adapted with permission from Ref. [16]. Copyright (2005) American Chemical Society.) (c) Comparison between flow behavior in the liquids slugs of Taylor flow in straight and meandering channel. (Adapted from Ref. [27] with permission of The Royal Society of Chemistry.)

Bretherton [28]:

$$\delta_{\text{film}} = 0.67\, d_t\, Ca_L^{\frac{2}{3}} \quad \text{for} \quad Ca_L \leq 3 \cdot 10^{-3} \tag{7.2}$$

Aussillous and Quere [29]:

$$\delta_{\text{film}} = d_t \frac{0.67 Ca_L^{2/3}}{1 + 3.35 Ca_L^{2/3}} \quad \text{for } Ca_L < 1 \tag{7.3}$$

It is important to note that the definition of $Ca$ is based on bubble velocity ($u_b$). The bubble velocity in vertical capillaries was found to depend on the two-phase superficial velocity $u$ and the capillary number ($\text{Ca}_{\text{L,u}}$), which is calculated with the two-phase superficial velocity. On the basis of the experimental results obtained with different capillary diameters and liquids, Liu *et al.* [16] proposed the following relationship:

$$u_b = \frac{u}{1 - 0.61 \cdot Ca_{L,u}^{0.33}}; \text{ with } Ca_{L,u} = \frac{\mu_L u}{\sigma}; \; u = u_G + u_L \tag{7.4}$$

$u_G$, $u_L$ are the superficial velocities of the gas and the liquid, respectively. The bubble velocity is related to the superficial gas velocity by:

$$u_b = \frac{u_G}{\varepsilon_G}; \quad \varepsilon_G \text{ is the volumetric fraction of the gas phase} \tag{7.5}$$

The bubble velocity and film thickness is estimated in Example 7.1.

**Example 7.1: Bubble velocity and wall film thickness**

Estimate the capillary number for air–water system and wall film thickness for two-phase superficial velocity between $0.05 \leq u \leq 1.2\ \mathrm{m\,s^{-1}}$ and $u_G/u_L = 1$. The capillary diameter is $d_t = 1.0$ mm. The physical properties are summarized in Table 7.2.

**Table 7.2** Physical properties of the air/water system.

| | Density, $\rho$ (kg m$^{-3}$) | Viscosity, $\mu$ (Pa s) | Interfacial tension, $\sigma$ (N m$^{-1}$) |
|---|---|---|---|
| Air | 1.2 | $1.78 \times 10^{-5}$ | — |
| Water | 998.2 | $10^{-3}$ | 0.072 |

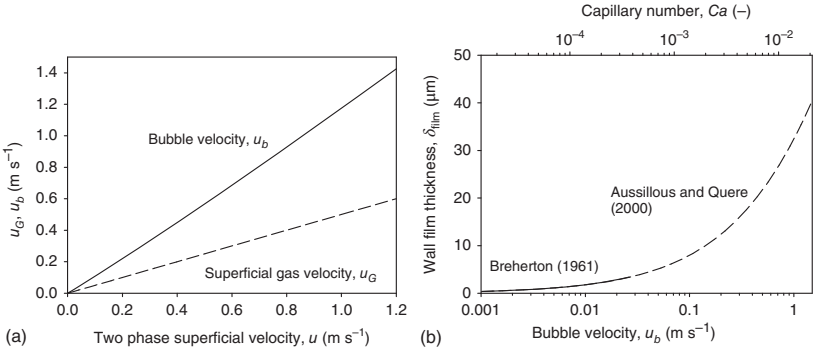


**Figure 7.7** (a) Estimated bubble velocity versus two-phase superficial velocity; (b) liquid wall film thickness versus bubble velocity and capillary number.

***Solution:***

Using Equation 7.4, the bubble velocity can be estimated. In Figure 7.7 the bubble velocity and the superficial gas velocity is plotted as the function of the two-phase superficial velocity *u*. It is evident that the bubble velocity is much higher than the calculated gas velocity and exceeds even the two-phase superficial velocity. Figure 7.7b shows the estimated thickness of the liquid wall film $\delta_{\mathrm{film}}$ based on Equations 7.2 and 7.3. For low capillary number

($Ca \leq 3 \cdot 10^{-3}$) both relations result in the same values. Aussillous and Quere corrected Bretherton's relation to fit experimental results obtained for higher capillary numbers.

For noncircular channels, the general practice is to use the hydraulic diameter $d_h$ in the above equation though the situation is more complex. A long bubble in a circular tube acts as a tight-fit piston, while in a polygonal tube, particularly at higher flow velocities, it behaves like a leaky piston. The fluid prefers to bypass the bubble through the corners because of the large drag of the bubble. The corner flow could be an order faster than the bubble that loses symmetry with the microchannel axis. This transition in square channel occurs at $Ca_L \cong 0.04$ [30].

#### 7.3.1.3 Slug Bubbly Flow

The slug bubbly flow is a transition regime that occurs between bubbly and Taylor flows. In most of the literature, this regime is considered as a part of Taylor flow. However, it differs from Taylor flow because of the presence of small bubbles in the continuous liquid phase as shown in Figure 7.8a. Small and elongated bubbles are separated from each other by liquid slugs. This regime is relatively unstable and the transition from Taylor flow to slug bubbly flow occurs by increasing the liquid flow rate at constant gas flow rate.

#### 7.3.1.4 Churn Flow

Churn flow occurs at very high gas velocities. It consists of very long gas bubbles and relatively small liquid slugs as shown in Figure 7.8b. In churn flow, because of high gas velocity, a wave or ripple motion is often observed at the bubble tail with tiny gas bubbles entrained in the liquid slug [16]. In a microchannel, two types of churn flow are observed: either showing streaks and swirls that trail the gas slug or interfacial structures resembling a serpentine-like gas core moving through the

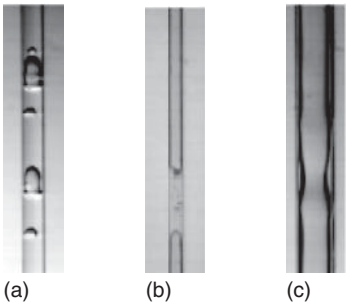


**Figure 7.8** Flow regime at elevated gas and liquid velocities in vertical capillary. (a) Slug-bubbly flow, (b) churn flow, (c) annular flow. (Adapted with permission from Ref. [16]. Copyright (2005) American Chemical Society.)

**Table 7.3** Difference between slug and parallel flow in fluid-fluid MSR.

| Slug or Taylor flow | Parallel flow |
|---|---|
| Slug flow is a flow of a series of slugs (plugs) of one phase separated by the other | Parallel flow is a flow of two parallel streams |
| Each slug serves as an individual processing subvolume. In liquid–liquid systems, one phase acts as continuous while other discrete | Both phases are continuous |
| Mass transport is because of convection within each slug and diffusion between two adjacent slugs | Mass transfer is because of diffusion only |
| Relatively higher interfacial area, which can be changed in a given reactor by varying the flow rates | Relatively low interfacial area and is constant in a given microchannel |
| Intensity of internal circulations increases with flow and thus diffusive penetration between two phases | No effect of flow velocity on diffusive penetration |
| Downstream separation is difficult | Downstream separation is relatively easy |

liquid [31, 32]. With increased flow velocity, it leads to the merging of the bubbles that is often referred to as *slug annular flow* [32].

#### 7.3.1.5 Annular and Parallel Flow

In a microchannel, at excessively high gas velocity and very low liquid velocity, two flow regimes are observed: annular and parallel flow. The former is produced in a flow symmetric contacting (concentric) geometry while the latter is formed in flow asymmetric geometries (T or Y type). In an annular flow, a continuous gas phase is present in the central core with the liquid phase being displaced to form an annulus between the wall and the gas phase [16] (Figure 7.8c), while in parallel flow, both phases flow parallel.

The comparison of annular (or parallel) flow with Taylor flow, another stable regime, is presented in Table 7.3. The additional advantages of slug flow over parallel flow allow it to use for wide range of applications.

There are some case-specific applications where annular flow is used. Falling film reactor is one of the examples. In this case, the liquid flows downward because of gravity in the form of film and gas flows through the open space, which lies in the top cover of the housing.

### 7.3.2 Liquid–Liquid Flow Patterns

The flow regimes observed in liquid–liquid flow in microchannels such as drop, slug, slug-drop, deformed interface, annular, parallel, and dispersed flow are depicted in Figure 7.9.

The different flow regimes are presented and discussed in the following sections.

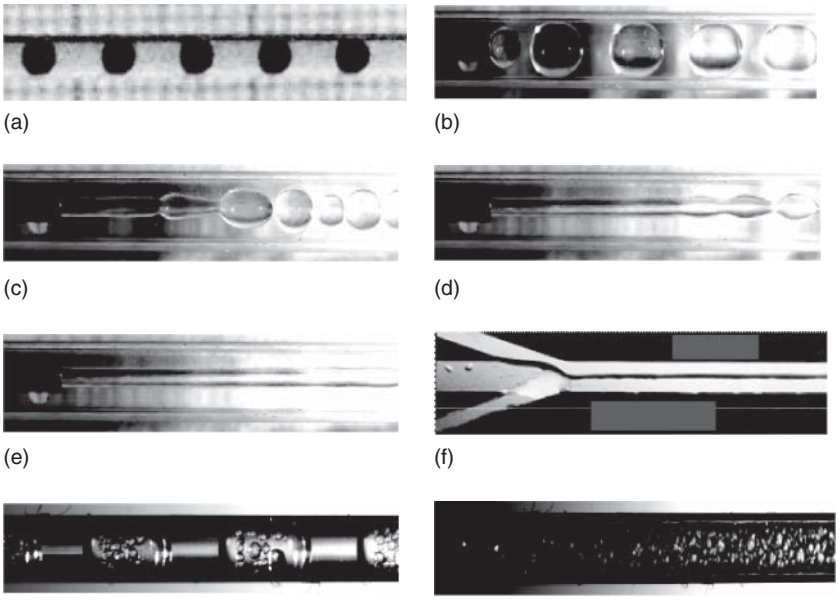


**Figure 7.9** Flow regimes observed for liquid–liquid systems in microstructured reactors. (a) Drop flow in a Y-junction capillary microchannel, (b) Slug flow in a concentric microchannel, (c) Slug-drop flow in a concentric microchannel, (d) Deformed interface flow in a concentric microchannel, (e) Annular flow in a concentric microchannel, (f) Parallel flow in a wedge-shaped microchannel, (g) Slug-dispersed flow in a caterpillar mixer attached capillary, (h) Dispersed flow in a caterpillar mixer ($u = 3.2\ \mathrm{m\ s^{-1}}$) attached capillary [33]. (Adapted with permission from Elsevier.)

#### 7.3.2.1 **Drop Flow**

This flow is identical to the bubbly flow of gas–liquid systems. It is characterized by the drops with diameters less than or equal to the microchannel diameter. In a microchannel, this flow pattern typically occurs at relatively high continuous flow velocities and low dispersed phase velocities. The drop size is restricted by channel dimensions. By varying the microchannel dimensions, the flow regimes can be changed from drop flow to slug flow and vice versa [12].

#### 7.3.2.2 **Slug Flow**

In this flow regime, one liquid flows as a continuous phase while the other flows in the form of slugs (droplets) longer than the diameter of the microchannel. In this case, the surface tension between one of the liquids and the wall material is higher than the interfacial tension between two liquids. The high surface tension phase flows in the form of enclosed slugs while the other phase flows as a continuous phase forming a thin wall film of a few micrometers in size. If the flow does not satisfy this condition, then both liquids flow alternatively without forming a wall

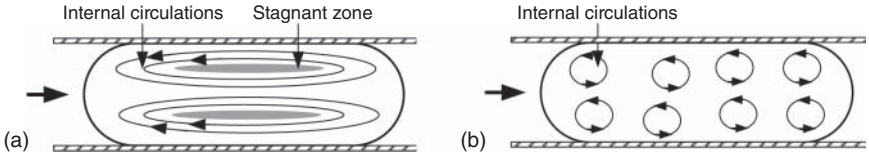


**Figure 7.10** Schematics of internal circulations within the slug. (a) Without surfactant and (b) with surfactant added to one of the liquids.

film. In both the cases, the surface tension at the liquid–liquid interface must be sufficiently high in order to avoid the destruction of slugs by the shear [34]. This flow pattern occurs at relatively low and approximately equal flow rates of both liquids where interfacial forces dominate. This is a commonly observed stable flow regimes in microchannels [35–37].

As both phases move alternatively, each slug of the dispersed phase serves as an individual processing subvolume, which is highly regular (see Figure 7.9b) and guarantees well-defined interfacial area for mass transfer. A key feature of this type of flow is the ability to manipulate the two principal transport mechanisms: convection within the individual slug of each liquid phase (Figure 7.10a) and interfacial diffusion between adjacent slugs of different phases. The shear between capillary wall and dispersed slug axis generates intense internal circulations within the slug, which in turn reduces the thickness of interfacial boundary layer and thereby augments the diffusive penetration. The mass transfer behavior depends on the slug geometry and circulation patterns, which vary with the physical properties of liquids as well as with operating parameters such as flow rates, mixing element geometry, and the capillary dimensions. These internal circulations can be hindered by adding surface active agents, for example, cationic surfactant, that accelerate the movement of the interface resulting in local convection pattern. Thus, the mass transfer performance can be increased.

#### 7.3.2.3 Slug-Drop Flow

In this regime, the dispersed phase flows in the forms of irregular slugs and drops. This flow occurs during the transition to or from slug flow: either at low volumetric flow rate of the dispersed phase compared to the continuous phase, or at the flow rate higher than slug flow.

#### 7.3.2.4 Deformed Interface Flow

This flow regime is also referred to as *intermittent* or *irregular flow*. At relatively high flow velocity, the dispersed phase flows to a certain distance in the form of either parallel or annular flow and then produces irregular droplets. The length of the parallel flow region increases with flow velocity. If the volumetric flow rate of the dispersed phase is higher as compared to the continuous phase, then the slugs of the former flow close to each other. The deformation of hemispherical caps of the slug becomes more pronounced and it tends to form bridges between

adjacent slugs, which may lead to the formation of larger slugs by coalescence. This regime is less stable and acts as a transition between the slug-drop flow regime and the parallel flow.

#### 7.3.2.5 Annular and Parallel Flow

As in gas–liquid systems, this flow is formed based on the type of microchannel geometry used: flow symmetric geometry forms annular flow, while flow asymmetric forms parallel flow. This flow regime is observed at elevated flow rates in the microchannel without static internals – the higher the flow velocity, the better the stability. The shear force of the continuous phase is dominant over the surface tension force and, therefore, the dispersed phase flows straight forming annular or parallel flow.

The parallel flow can also be formed at low flow velocity, especially in rectangular cross section microchannel, if the interfacial tension between two fluids is very low, for example, wedge-shaped parallel flow contactor [38], or modifying the wettability of the channel walls (see Figure 7.28). The flow could be stabilized by placing membranes or sieve plates inside the channels [9, 39].

#### 7.3.2.6 Slug-Dispersed Flow

To create fine dispersion in microcapillaries, a micromixer (e.g., caterpillar mixer) needs to be attached upstream. At elevated flow velocity the static internals create dispersion, and as a result, part of the continuous phase flows in the form of small droplets in the dispersed phase.

#### 7.3.2.7 Dispersed Flow

This flow regime is observed when the flow velocity is further increased in the microchannel with structured internals. Very fine droplets of one phase into the other are created.

The flow regime transition in liquid–liquid flow could be explained by applying the dimensionless numbers. The flow patterns in liquid–liquid systems depend on the volume fraction of dispersed phase ($\varepsilon_D$) and hydraulic diameter of the microchannel in addition to the dispersed phase Reynolds number

$$Re_D = \frac{u_D d_h}{\nu_D} \tag{7.6}$$

Here $u_D$ is the superficial velocity of the dispersed phase.

The investigation of volume fraction of dispersed phase in the microchannel is not trivial. Equating volume fraction ($\varepsilon_D$) to volumetric flow fraction $\varphi_D = \dot{V}_D/(\dot{V}_D + \dot{V}_C)$, a new group, $Re_D d_h/\varepsilon_D$, is introduced to characterize the flow pattern of liquid–liquid systems in capillaries [40]. The following criteria were obtained for the toluene/water system:

$$\begin{aligned}
&\text{Surface tension dominated (slug flow)}: Re_D \cdot d_h/\varepsilon_D < 0.1 \ \text{(m)} \\
&\text{Transition (slug-drop, deformed interface flow)}: 0.1(\text{m}) < Re_D \cdot d_h/\varepsilon_D < 0.35(\text{m}) \\
&\text{Inertia dominated region (annular, parallel flow)}: Re_D \cdot d_h/\varepsilon_D > 0.35\,(\text{m})
\end{aligned} \tag{7.7}$$

As the criterion possesses dimension, it is advised to use SI units. It is important to note that the above criterion is valid for microchannels without structured internals.

**Example 7.2: Flow pattern of a liquid-liquid system**

Investigate the proportion of two fluids in a microchannel with circular cross section to operate under slug flow regime for extraction of acetone from continuous water to dispersed toluene with $\dot{V}_D = 2\,\mathrm{ml\,min^{-1}}$.

**Data:** $\rho_{\text{toluene}} = \rho_D = 867\,\mathrm{kg\,m^{-3}}$, $\mu_{\text{toluene}} = \mu_D = 0.6 \cdot 10^{-3}\,\mathrm{kg\,ms^{-1}}$, $\rho_{\text{water}} = \rho_C = 998.2\,\mathrm{kg\,m^{-3}}$, $\mu_{\text{water}} = \mu_C = 1 \cdot 10^{-3}\,\mathrm{kg\,ms^{-1}}$, $\sigma = 0.036\,\mathrm{N\,m^{-1}}$.

***Solution:***

According to the criteria proposed in Equation 7.7, the stable slug flow regimes is observed at $Re_D \cdot d_h / \varepsilon_D < 0.1$ m. Thus, equating the term to 0.1, one can estimate the diameter of a microchannel. Thus,

$$\frac{\rho_D u_D d_h}{\mu_D \varphi_D} d_h = 0.1\,\mathrm{m}$$

As the velocity and dimensions of microchannel are not given, they can be written in terms of flow rate as $\dot{V}_D = \pi d_h^2 u_D / 4$ or $u_D d_h^2 = 4\dot{V}_D / \pi$ resulting in

$$\frac{\rho_D}{\mu_D \varphi_D} \frac{4\dot{V}_D}{\pi} = 0.1\,\mathrm{m}$$

$$\Rightarrow \varphi_D = \frac{4 \cdot \dot{V}_D \cdot \rho_D}{0.1 \cdot \pi \cdot \mu_D} = \frac{4 \cdot \frac{2 \cdot 10^{-6}}{60} \cdot 867}{0.1 \cdot \pi \cdot 0.6 \cdot 10^{-3}} = 0.61$$

Thus, volumetric flow fraction of toluene is 0.61 resulting in water flow fraction of 0.39, which is necessary to obtain slug flow behavior.

## 7.4 Mass Transfer

For the applications involving multiphase reactions and separations, the mass transfer of a solute from one phase to the other or of a pure phase into another is necessary. The mass transfer rates are different in nonreactive and reactive chemical systems. In nonreactive (separation/extraction) case, the mass is transferred from the phase with higher chemical potential (partial pressure or concentration) to the lower until the equilibrium is reached. In reactive systems, the mass transfer is enhanced because of the consumption of transferring species from one phase to the other.

### 7.4.1 Mass Transfer Models

Different approaches have been used to model mass transfer performance of reactors. They comprise two main parts: the micromodel, describing the mass transfer between two phases, and the macromodel, describing the mixing pattern within the individual phase. The micromodels assume two types of interfacial behavior: stagnant films or dynamic absorption in small elements at the contact surface.

Let us consider the gas–liquid mass transfer. In the stagnant film model, it is postulated that mass transfer proceeds via steady-state molecular diffusion in a hypothetical stagnant film at the interface with thickness $\delta_{\text{int}}$ while the bulk of the liquid is well mixed [41]. Though this model incorporates the important features of the real system and is simple to use, the prediction of hydrodynamic parameter $\delta_{\text{int}}$ is difficult as it depends on the contactor geometry, liquid agitation, and physical properties.

The penetration model, proposed by Higbie [42], assumes that every element of surface is exposed to gas for the same time ($\theta_c$) before being replaced by a liquid of bulk composition. The exposure time ($\theta_c$) is investigated using hydrodynamic properties such as interface velocity and its length.

Film and penetration models are most commonly used defining the liquid-side mass transfer coefficients ($k_L$) as follows:

$$\text{Penetration model}: k_L = 2\sqrt{\frac{D_m}{\pi\theta_c}}$$

$$\text{Film model}: k_L = \frac{D_m}{\delta_{\text{int},II}} \tag{7.8}$$

where $D_m$ is molecular diffusivity of solute in liquid phase and $\delta_{\text{int, }II}$ is hypothetical interfacial film thickness in the liquid phase.

The application of suitable models to various systems must be determined on a case-by-case basis. This could be judged from the behavior of experimental mass transfer coefficient with respect to the contact time of two phases. For dynamic systems, the penetration model is physically more realistic than the stagnant film model. However, the mixing in different phases is important to describe the overall mass transfer performance, and, therefore, the above models are usually combined with fluid flow models, which includes detailed flow description.

Further, a film-penetration model is also used to include resistance on both sides, yielding a two-parameter model combining the stagnant film and penetration models, as shown in Figure 7.11b [43, 44].

Frequently applied micromodels assume the presence of a liquid bulk. However, some systems are without liquid bulk as in falling film reactors where a very thin layer of liquid flows over a solid surface.

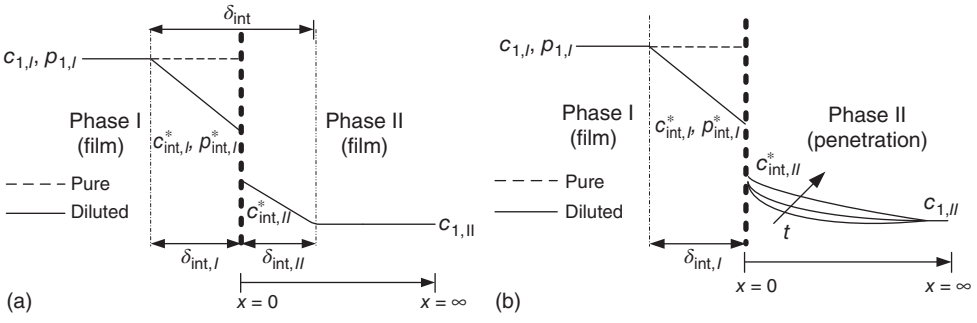


**Figure 7.11** Schematic representation of concentration profiles in gas–liquid and liquid–liquid systems assuming (a) two-film model and (b) combined film-penetration model. Here, phase I is gas for gas–liquid and liquid for liquid–liquid systems while phase II is always a liquid forming the continuous phase. The superscript * indicates the equilibrium values while subscript *int* indicates interface values.

### 7.4.2
### Characterization of Mass Transfer in Fluid–Fluid Systems

When a solute transfers from phase I (gas phase) to phase II (liquid) with the phase equilibrium at the interface, the individual transfer rates at steady state can be written as

$$J_I = k_G(p_{1,I} - p^*_{\text{int},1,I}) = J_{II} = k_L\left(\frac{p^*_{\text{int},1,II}}{H} - c_{1,II}\right) \tag{7.9}$$

where $p_{1,I}$ is partial pressure of a gaseous solute while $k_G$ and $k_L$ are the gas and liquid phase mass transfer coefficients, respectively. The ratio of partial pressure of a solute in phase I to its corresponding bulk concentration in phase II at equilibrium is called as *Henry's constant* ($H$).

Equating both fluxes ($J_I = J_{II} = J$) and deriving the overall mass transfer coefficient ($k_{ov}$), Equation 7.9 can be written as

$$J = \frac{Hk_Gk_L}{Hk_G + k_L}\left(\frac{p_{1,I}}{H} - c_{1,II}\right) = k_{ov}\left(\frac{p_{1,I}}{H} - c_{1,II}\right)$$

$$\text{where, } k_{ov} = \frac{Hk_Gk_L}{Hk_G + k_L} = \frac{1}{\frac{1}{Hk_G} + \frac{1}{k_L}} \tag{7.10}$$

The mass transfer performance of any reactor for a given system (reactor/contactor and solute) is characterized by overall volumetric mass transfer coefficient ($k_{ov}a$).

A microstructured reactor is an open system and its performance can be compared to ideal plug flow or backmixed flow reactor. Generally, continuous flow microstructured reactors are considered as ideal plug flow reactors with narrow residence time distribution (see Chapter 3). In the case of slug or Taylor flow, both fluids flowing through microchannels exchange mass between the same compartments (e.g., between same gas and liquid slugs), and, therefore, one driving force

is required to define the mass transfer rate. For a solute transferring from phase I (gas) to II (liquid) and assuming that the resistance lies in the liquid phase (phaseII), the change of its concentration in the liquid with respect to residence time ($\tau$) can be written as:

$$\frac{dc_{1,II}}{d\tau} = J_{II}a = k_L a(c^*_{1,II} - c_{1,II}); \text{with } k_L \cong k_{ov} \tag{7.11}$$

where $c^*_{1,II}$ is the equilibrium concentration in phase II corresponding to bulk concentration in phase I. On integration of the above equation from initial time ($\tau = 0$) to residence time ($\tau$) and concentration from inlet ($c^{in}_{1,II}$) to outlet ($c^{out}_{1,II}$), the overall volumetric mass transfer coefficient ($k_{ov}a$) becomes

$$k_{ov}a = \frac{1}{\tau} \ln\left(\frac{c^*_{1,II} - c^{in}_{1,II}}{c^*_{1,II} - c^{out}_{1,II}}\right) \tag{7.12}$$

where $a$ is the specific interfacial area, defined as the interfacial area per unit volume of the dispersed phase.

### 7.4.3 Mass Transfer in Gas–Liquid Microstructured Devices

Mass transfer takes place from the gas phase to the liquid phase as well as in the reverse direction and chemical reactions may occur in the gas and/or in the liquid phase, respectively. The mass transfer performance of any gas–liquid reactor depends on two-phase flow patterns that define the interfacial area.

The mass transfer performance of gas–liquid microstructured reactors has been investigated under different flow regimes, which are discussed in the following section.

#### 7.4.3.1 Mass Transfer in Taylor Flow

The experimental works on investigation of gas–liquid mass transfer in microstructured reactors are listed in Table 7.4. Most of the experimental results were obtained for Taylor flow in capillaries with diameters between 1 and 3 mm. The influence of experimental conditions on mass transfer is very complex. This explains why most of the published relations describing gas–liquid mass transfer are empirical.

A relatively simple model to describe the gas–liquid mass transfer in circular channels with slug flow pattern was proposed by van Baten and Krishna [47]. For their fundamental model the authors considered an idealized geometry of the Taylor bubbles as shown in Figure 7.12. The bubbles consist of two hemispherical caps and a cylindrical body. The Higbie penetration model was applied to describe the mass transfer process of a compound from the gas phase to the liquid (Equation 7.8). For a rising bubble, the liquid will flow along the bubble surface of the cap. The average distance

**Table 7.4** Literature on gas–liquid mass transfer in Taylor flow.

| Regime and system | Conditions and definition | Global volumetric mass transfer coefficient |
|---|---|---|
| Irandoust *et al.* [45] | | |
| Slug(Taylor) flow – vertical reactor Absorption of oxygen from air into water, ethanol, and ethylene glycol (EG) | $d_t = 1.5, 2\,\text{mm}$ $L = 0.6\,\text{m}$ $u = 0.092-0.56\,\text{m s}^{-1}$ | $k_{ov}a = 0.01-0.29\,\text{s}^{-1}$ $k_{ov}a = 4\frac{\delta(d_h-\delta_{film})uy_m+D_m\,Sh_L\,d_b}{d_t^2 L_{UC}}\;y_m = \frac{c_m-c_2^{in}}{c_2^*-c_2^{in}}$ (7.13) |
| Bercic and Pintar [26] | | |
| Slug(Taylor) flow – vertical reactor Nonreacting system Methane–water | $d_t = 1.5, 2.5, 3.1\,\text{mm}$ $L = 1.12\,\text{m}$ $u = 0.02-0.43\,\text{m s}^{-1}$ | $k_{ov}a = 0.005-0.115\,\text{s}^{-1}$ $k_{ov}a = \frac{0.111\,(u_L+u_G)^{1.19}}{((1-\varphi_G)L_{UC})^{0.57}}$ (7.14) |
| Vandu *et al.* [46] | | |
| Slug flow – vertical reactor Nonreacting system Air–water | $d_t = 1, 2, 3\,\text{mm}$ $L = 0.2-1.4\,\text{m}$ $u = 0.22-0.43\,\text{m s}^{-1}$ | $k_{ov}a = 0.08-0.47\,\text{s}^{-1}$ $k_{ov}a = 4.1\sqrt{\frac{D_m u_G}{L_{UC}}}\frac{1}{d_t}$ (7.15) |
| Yue *et al.* [32] | | |
| Slug flow, slug annular, churn flow Reacting system $CO_2$/buffer solution of 0.3 M $NaHCO_3$, 0.3 M $Na_2CO_3$, NaOH | $d_h = 667\,\mu\text{m}$ $u_G = 0-2\,\text{m s}^{-1}$ $u_L = 0.09-1\,\text{m s}^{-1}$ | $k_{ov}a = 0.3-21\,\text{s}^{-1}$ Slug flow: $Sh_L a d_h = 0.084 Re_G^{0.213} Re_L^{0.937} Sc_L^{0.5}$ (7.16) $Sh_L = \frac{k_L d_h}{D_m}; Re_i = \frac{\rho_i u_i d_h}{\mu_i}; Sc_L = \frac{\mu_L}{\rho_L D_m}; i = G \text{ or } L$ |

traveled by the liquid packets will be one-half of the bubble circumference: $l_c = \pi \cdot d_b/2$. As the thickness of the wall film is small compared to the capillary diameter (see Figure 7.7), it can be neglected and we obtain $l_c = \pi \cdot d_t/2$. The average contact time of the liquid with the bubble cap will be:

$$\theta_{c,\text{cap}} = \frac{\pi \cdot d_t}{2 \cdot u_b}; \text{with } u_b \text{ the bubble velocity} \tag{7.17}$$

The penetration model for mass transfer yields:

$$k_{L,\text{cap}} = 2\sqrt{\frac{D_m \cdot u_b \cdot 2}{\pi^2 \cdot d_t}} = \frac{2\sqrt{2}}{\pi}\sqrt{\frac{D_m \cdot u_b}{d_t}} \tag{7.18}$$

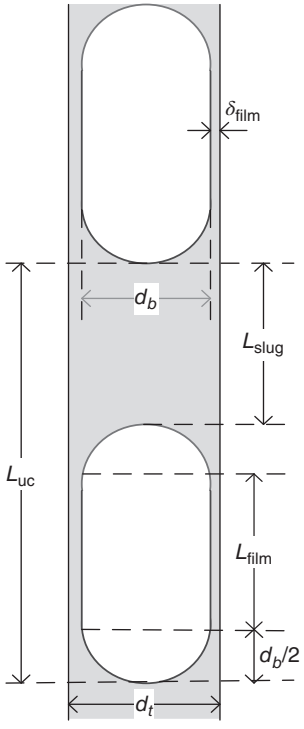


**Figure 7.12** Taylor bubble (schematic).

The volumetric mass transfer of the bubble caps is obtained by multiplying the mass transfer coefficient with the specific surface of the two caps referred to the volume of a cell unit $V_{UC}$.

$$a_{cap} = \frac{2A_{cap}}{V_{UC}} = \frac{2\pi d_b^2/2}{\pi/4 \cdot d_b^2 \cdot L_{UC}} = \frac{4}{L_{UC}} \tag{7.19}$$

$$k_{L,cap}a_{cap} = \frac{2\sqrt{2}}{\pi}\sqrt{\frac{D_m \cdot u_b}{d_t}} \cdot \frac{4}{L_{UC}} \tag{7.20}$$

Accordingly, the penetration model can be used to predict the film mass transfer coefficient.

$$k_{L,film} = \frac{2}{\sqrt{\pi}}\sqrt{\frac{D_m}{\theta_{c,film}}} \tag{7.21}$$

The specific interfacial area of the film $a_{film}$ can be approximated with [46]:

$$a_{film} = \frac{4 \cdot \varepsilon_G}{d_t}; \text{with } \varepsilon_G \text{ the gas hold-up (volume fraction)} \tag{7.22}$$

In summary, the gas–liquid mass transfer in Taylor flow has two contributions (see Figure 7.6b): (i) the caps (assumed to be hemispherical) at both ends of the bubble and (ii) the liquid film surrounding the lateral sides of the bubble. Considering these two contributions and assuming resistance in the liquid phase, the relationship for the overall mass transfer coefficient ($k_{ov}a \cong k_La$) is given in the following:

$$k_La = k_{L,\text{cap}}a_{\text{cap}} + k_{L,\text{film}}a_{\text{film}}$$

$$k_La = 2\sqrt{\frac{2D_mu_b}{\pi^2 d_t}}\frac{4}{L_{\text{UC}}} + 2\sqrt{\frac{D_m}{\pi\theta_{c,\text{film}}}}\frac{4\varepsilon_G}{d_t} \tag{7.23}$$

The model provided excellent agreement with computational fluid dynamic simulations for capillaries with 1.5, 2, and 3 mm diameters and idealized bubble geometry as shown in Figure 7.12 [47]. The major contribution to mass transfer is in the film ($k_{L,\text{film}}a_{\text{film}}$) as long as the concentration of the solute is low in the liquid film. Under these conditions, the model (Equation 7.23) can be simplified taking only the film contribution into account as follows [46]:

$$k_La \cong \frac{8}{\sqrt{\pi}}\sqrt{\frac{D_m}{\theta_{c,\text{film}}}}\frac{\varepsilon_G}{d_t} = 4.5\sqrt{\frac{D_mu_b}{L_b}}\frac{\varepsilon_G}{d_t};\ \theta_{c,\text{film}} = \frac{L_b}{u_b} \tag{7.24}$$

On the basis of the experimental studies of Taylor flow in capillaries of Heiszwolf *et al.* [48], an empirical correlation for estimating liquid slug lengths ($L_{\text{slug}}$) was proposed by Kreutzer [30] :

$$L_{\text{slug}} = d_t\frac{\varepsilon_L}{-0.00141 - 1.55\varepsilon_L^2\ln(\varepsilon_L)};\ \text{with}\,\varepsilon_L = (1-\varepsilon_G) \tag{7.25}$$

The bubble length and the length of the liquid slug can be approximated with [46]:

$$L_b \cong L_{\text{UC}}\cdot\varepsilon_G;\ L_{\text{slug}} \cong L_{\text{UC}}\cdot(1-\varepsilon_G) \tag{7.26}$$

In Equation 7.24 we replace the bubble length with $L_b \cong L_{\text{UC}}\cdot\varepsilon_G$ and the bubble rise velocity with the superficial gas velocity (Equation 7.5) $u_b = u_G/\varepsilon_G$ and obtain:

$$k_La \cong 4.5\sqrt{\frac{D_mu_G}{\varepsilon_G^2 L_{\text{UC}}}}\frac{\varepsilon_G}{d_t} = 4.5\sqrt{\frac{D_mu_G}{L_{\text{UC}}}}\frac{1}{d_t} \tag{7.27}$$

A plot of experimental $k_La$ values versus $\frac{\sqrt{D_mu_G/L_{\text{UC}}}}{d_t}$ showed a straight line with a slop of 4.5, thus confirming the theoretical value from the model for the film contribution. The agreement between the model and the experiment is reasonably good for both circular and square capillaries showing dependency of $k_La$ on capillary diameter. The validity of the model was found to be well for $\sqrt{((\mathrm{u}_G + \mathrm{u}_L)/L_{\text{slug}})} > 3$, which corresponds to a short film contact time and a dominant film contribution [46]. Below this range, the film contribution to mass transfer diminishes as the liquid in the film begins to approach saturation.

A simple criterion for the effectiveness of the interfacial film area was proposed by Pohorecki [49]. The criterion is based on the characteristic diffusion time of the species in the film $t_{D,\,\mathrm{film}}$ and the film contact time $\theta_{c,\,\mathrm{film}}$. For physical absorption, the film can be considered as far from saturation, if $\theta_{c,\,\mathrm{film}} \ll t_{D,\,\mathrm{film}}$. The criterium is summarized in Equation 7.28.

$$\frac{\theta_{c,\mathrm{film}}}{t_{D,\mathrm{film}}} = \frac{L_b}{u_b} \cdot \frac{D_m}{\delta^2_{\mathrm{film}}} \ll 1 \tag{7.28}$$

Estimation of mass transfer using equation 7.15 is demonstrated in Example 7.3.

**Example 7.3: Mass transfer in gas-liquid MSR**

Estimate the volumetric mass transfer coefficient in a Taylor flow capillary with an internal diameter of 1 mm and a volumetric gas flow of $\dot{V}_G = 2.71\,\mathrm{cm^3\,min^{-1}}$ and a volumetric liquid flow of $\dot{V}_L = 2.0\,\mathrm{cm^3\,min^{-1}}$. Use the simplified model presented in Equation 7.27 and compare the values with those predicted with the empirical model Equation 7.14. Use the physical properties for air and water presented in Example 7.1. The molecular diffusion coefficient in the liquid phase is approximated with $D_m = 10^{-9}\,\mathrm{m^2\,s^{-1}}$.

***Solution:***

The superficial velocities of gas and liquid are given by $u_i = \dot{V}_i / A_{\mathrm{cs}}$ with $A_{\mathrm{cs}} = 7.85 \cdot 10^{-7}\,\mathrm{m^2}$, the cross section area.

*Superficial velocities:*

$$u = \frac{\dot{V}_G + \dot{V}_L}{A_{\mathrm{cs}}} = \frac{4.52 \cdot 10^{-8} + 3.33 \cdot 10^{-8}}{7.85 \cdot 10^{-7}} = 0.1\,\mathrm{m\,s^{-1}}\; u_G = 0.0575\,\mathrm{m\,s^{-1}};\; u_L = 0.0425\,\mathrm{m\,s^{-1}}$$

*Bubble rise velocity* (Equation 7.4):

$$u_b = \frac{u}{1 - 0.61 \cdot Ca_{L,u}^{0.33}};\ \text{with}\ Ca_{L,u} = \frac{\mu_L u}{\sigma} = \frac{10^{-3} \cdot 0.1}{0.072} = 1.39 \cdot 10^{-3}$$

$$u_b = \frac{0.1}{1 - 0.61 \cdot (1.39 \cdot 10^{-3})^{0.33}} = 0.107\,\mathrm{m\,s^{-1}}$$

*Volumetric fraction of the gas phase (gas hold-up)* Equations 7.5 *and* 7.26:

$$\varepsilon_G = \frac{u_G}{u_b};\ \ \varepsilon_G = \frac{0.0575}{0.107} = 0.537$$

*Slug length and length of a unit cell* (Equation 7.25):

$$L_{\mathrm{slug}} = d_t \frac{\varepsilon_L}{-0.00141 - 1.55\varepsilon_L^2 \ln(\varepsilon_L)};\ \text{with}\ \varepsilon_L = 1 - \varepsilon_G = 0.463$$

$$L_{\mathrm{slug}} = \frac{10^{-3} \cdot 0.463}{-0.00141 - 1.55 \cdot 0.463^2 \cdot \ln(0.463)} = 1.82 \cdot 10^{-3}\,\mathrm{m}$$

$$L_{UC} \cong \frac{L_{slug}}{(1-\varepsilon_G)} = \frac{1.82 \cdot 10^{-3}}{0.463} = 3.9 \cdot 10^{-3}\,\mathrm{m}$$

*Volumetric mass transfer coefficient* (Equation 7.27) [46]:

Equation 7.27 is applicable if: $\sqrt{((u_G + u_L)/L_{slug})} > 3$; $\sqrt{(0.1/(1.82 \cdot 10^{-3}))} = 7.4$

$$k_L a \cong 4.5\sqrt{\frac{D_m u_G}{L_{UC}}}\frac{1}{d_t} = 4.5\sqrt{\frac{10^{-9} \cdot 0.0575}{3.9 \cdot 10^{-3}}}\frac{1}{10^{-3}} = 0.546\,\mathrm{s}^{-1}$$

*Volumetric mass transfer coefficient estimated with the empirical equation* (Equation 7.14) [26]:

$$k_{ov}a = \frac{0.111\,(u_L + u_G)^{1.19}}{((1-\varepsilon_G)L_{UC})^{0.57}} = \frac{0.111\,(0.1)^{1.19}}{(0.463 \cdot 3.9 \cdot 10^{-3})^{0.57}} = 0.262$$

**Remark:** Comparing the estimation based on the widely used empirical Equations 7.14 and the semi-empirical Equation 7.27, the latter predicts a roughly two times higher volumetric mass transfer coefficient. This may be because of the fact that Equation 7.14 does not include the capillary diameter. In general, predictions must be taken with caution because the two-phase systems are complex and none of the models include all practical experimental conditions.

#### 7.4.3.2 Mass Transfer in Slug Annular and Churn Flow Regime

The mass transfer performance under slug annular and churn flow regime is depicted in Table 7.5. From the reported values of mass transfer coefficients, it is observed that $k_L a$ is higher in churn flow compared to Taylor flow. However, the flow irregularity and low stability of these regimes limit their use for mass transfer.

**Table 7.5** Operating conditions used for mass transfer under churn flow regime by Yue *et al.* [32].

| Regime and system | Conditions and definition | Global volumetric mass transfer coefficient |
|---|---|---|
| Slug annular/churn flow<br>Reacting system<br>$CO_2$/buffer solution of 0.3 M $NaHCO_3$, 0.3 M $Na_2CO_3$,NaOH | $d_h = 667\,\mu\mathrm{m}$<br>$u_G > 2\,\mathrm{m\,s^{-1}}$<br>$u_L > 0.5\,\mathrm{m\,s^{-1}}$ | Physical absorption<br>Slug annular and churn flow:<br>$Sh_L a d_h = 0.058\,Re_G^{0.344}\,Re_L^{0.912}Sc_L^{0.5}$<br>$Sh_L = \frac{k_L d_h}{D_m}$; $Re_i = \frac{\rho_i u_i d_h}{\mu_i}$; $Sc_L = \frac{\mu_L}{\rho_L D_m}$;<br>$i = G \text{ or } L$ |

#### 7.4.3.3 Mass Transfer in Microstructured Falling Film Reactors

In falling film contactors, a thin film is created by a liquid falling under the influence of gravity. The liquid flows over a solid support, which is normally a thin wall or a stack of pipes. In conventional falling film devices, a film with a thickness of 0.5–3 mm is generated. This rather thick liquid film results in a significant mass transfer resistance for gaseous reactants. Furthermore, the film flow becomes unstable at high throughputs, and it may break up into rivulets, fingers, or droplets.

These problems can be overcome by microstructuring the solid wall. The microstructured falling film reactor consists of open microchannels, which are typically less than 1 mm wide, about 100 µm deep, and about 80 mm long. The channels are separated by 100 µm wide walls (Figure 7.13). Inflow and outflow of the liquid occur through boreholes that are connected via one large slit to numerous small orifices at the top of the channels. A structured heat-exchanger plate is inserted beneath the falling film plate for heat removal, and nearly isothermal operation can be achieved even for highly exothermic reactions such as the direct fluorination of organics with gaseous fluorine.

The main drawback of the microstructured falling film reactor is the short residence time of the liquid in the channels, which typically varies from 5 to 20 s, depending on the physical properties of the liquid and the operating conditions. The residence time can be increased by lengthening the channels or by decreasing the angle of descent, which can be achieved with a helicoidal microchannel falling film reactor. The residence time was found to be increased by a factor of about 50 in a microchannel when the angle of descent was decreased from 90° to 7.5° [14].

The mass transfer data on falling film microstructured reactor are presented in Table 7.6.

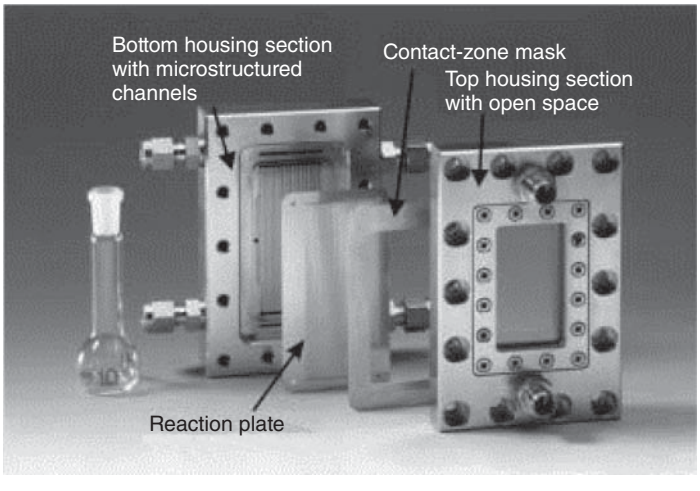


**Figure 7.13** A falling film microreactor with a viewing window [6]. (Adapted with permission from Wiley.)

**Table 7.6** Literature on mass transfer in falling film microchannel.

| Regime and system | Conditions and definition | Global volumetric mass transfer coefficient |
|---|---|---|
| Zhang *et al.* [50] | | |
| Complete falling flow regime<br>Nonreacting system $CO_2$/deionized water, 5.2 and 12 wt% EG solutions | Gas chamber depth – 0.8, 1.45, and 3.0 mm<br>3 PMMA 20 channels MSR (1000 µm × 300 µm × 60 mm)<br>$\dot{V}_G = 0.76, 3.05\,\mathrm{ml \cdot s^{-1}}$<br>$\dot{V}_L = 0.033 - 0.66\,\mathrm{ml \cdot s^{-1}}$<br>$T = 23–25°C$ | $k_L = 5.83 \cdot 10^{-5} – 13.4 \cdot 10^{*-5}\,\mathrm{m\,s^{-1}}$ for $Re_L < 150$<br>Empirical correlation:<br>$Sh_L = 0.0145\, Re_L^{0.69} Sc_L^{0.57}$ (7.29)<br>$Sh_L = \frac{k_L d_h}{D_m}$; $Re_L = \frac{4\delta_{\mathrm{film}} u_{\mathrm{film}}}{\nu_L}$;<br>$Sc_L = \frac{\nu_L}{D_m}$ |
| Sobieszuk *et al.* [51] | | |
| Reacting systems<br>Absorption of $CO_2$ to NaOH and monoethanolamine (MEA) solution | A stainless steel plate with 29 straight, open, vertical, parallel channels (78.3 mm × 0.3 mm × 0.6 mm)<br>$\dot{V}_G = 3.3\,\mathrm{ml \cdot s^{-1}}$ $\dot{V}_L = 0.255, 0.379, 0.627\,\mathrm{ml \cdot s^{-1}}$<br>Inlet concentration of $CO_2$ in $N_2$: 12–97% | $k_L = 7.22 \cdot 10^{-5} – 12.5 \cdot 10^{-5}\,\mathrm{m \cdot s^{-1}}$ |

In falling film microstructured reactors, Zhang *et al.* [50] proposed an empirical relation to estimate the mass transfer coefficient as shown in Equation 7 (Table 7.6).

The Reynolds number is defined as:

$$Re_L = \frac{4 u_{\mathrm{film}} \delta_{\mathrm{film}}}{\nu_L} \tag{7.30}$$

with the film velocity

$$u_{\mathrm{film}} = \frac{g \delta_{\mathrm{film}}^2}{3 \nu_L} \tag{7.31}$$

the film thickness

$$\delta_{\mathrm{film}} = \sqrt[3]{\frac{3 \dot{V}_L \nu_L}{n \cdot W \cdot g \cdot \sin\theta} \frac{\rho_L}{(\rho_L - \rho_G)}} \cong \sqrt[3]{\frac{3 \dot{V}_L \nu_L}{n \cdot W \cdot g \cdot \sin\theta}} \tag{7.32}$$

where *W, n, g,* and $\theta$ are width of microchannel, the number of microchannels, gravitational acceleration, and inclination angle from horizontal, respectively.

The mass transfer coefficient could be described with the penetration model supposing that the liquid residence time $\tau_L$ is very short compared to the diffusion time in the liquid film $t_D$.

$$Fo = \frac{\tau_L}{t_D} = \frac{L}{u_{\mathrm{film}}} \frac{D_m}{\delta_{\mathrm{film}}^2} \ll 1 \tag{7.33}$$

Example 7.4 investigates the mass transfer in microstructured falling film reactor.

**Example 7.4: Mass transfer in microstructured falling film reactor**

In a vertically placed 20 parallel channel microstructured falling film reactor of 60 mm length, 1 mm width, and 0.3 mm depth, gas and liquid flows with 46 ml · min$^{-1}$ and 3.6 ml · min$^{-1}$, respectively, estimate: (1) thickness of the wall film, (2) mean velocity of liquid film, (3) Fourier number, (4) Reynolds number, and (5) mass transfer coefficient, $k_L$.

Given: liquid kinematic viscosity $\nu_L = 8.97 \cdot 10^{-7}$ m$^2$ · s$^{-1}$ and Schmidt number $Sc_L = 452$.

***Solution:***

The first parameters are calculated using Equation 7.32

1) Wall film thickness for $n = 20$, $W = 1$ mm, $g = 9.81$ m · s$^{-2}$, $\dot{V}_L = 3.6$ ml · min$^{-1}$

$$\delta_{\text{film}} = \sqrt[3]{\frac{3\dot{V}_L \nu_L}{n \cdot W \cdot g \cdot \sin\theta} \frac{\rho_L}{(\rho_L - \rho_G)}} \cong \sqrt[3]{\frac{3\dot{V}_L \nu_L}{n \cdot W \cdot g \cdot \sin\theta}}$$

$$= \sqrt[3]{\frac{3 \cdot \frac{3.6 \cdot 10^{-6}}{60} \cdot 8.97 \times 10^{-7}}{20 \cdot 1 \cdot 10^{-3} \cdot 9.81 \cdot \sin 90}} = 9.37 \cdot 10^{-5}\,\text{m} = 93.7\,\mu\text{m}$$

2) Mean velocity of liquid film (Equation 7.31)

$$u_{\text{film}} = \frac{g\,\delta_{\text{film}}^2}{3\,\nu_L} = \frac{9.81 \cdot (93.7 \cdot 10^{-6})^2}{3 \cdot 8.97 \cdot 10^{-7}} = 0.03\,\text{m} \cdot \text{s}^{-1}$$

3) Fourier number: The diffusion coefficient required for Fo can be calculated from $Sc_L$ as $Sc_L = \nu_L / D_m$

$$D_m = \frac{\nu_L}{Sc_L} = \frac{8.97 \cdot 10^{-7}}{452} = 1.98 \cdot 10^{-9}$$

$$Fo = \frac{D_m L}{u_{\text{film}} \delta_{\text{film}}^2} = \frac{1.98 \cdot 10^{-9} \cdot 60 \cdot 10^{-3}}{0.03 \cdot (93.7 \cdot 10^{-6})^2} = 0.45$$

4) Reynolds number

$$Re_L = \frac{4 u_{\text{film}} \delta_{\text{film}}}{\nu_L} = \frac{4 \cdot 0.03 \cdot 93.7 \cdot 10^{-6}}{8.97 \cdot 10^{-7}} = 12.53$$

5) Mass transfer coefficient: The volumetric mass transfer coefficient is investigated using the correlation presented in terms of Sherwood number as a function of Reynolds number and Schmidt number in Table 7.6.

$$Sh_L = 0.0145\, Re_L^{0.69} Sc_L^{0.57}$$

$$= 0.0145 \times 12.53^{0.69} \times 452^{0.57} = 2.7$$

To investigate $k_L$ from $Sh_L$, the hydraulic diameter $d_h(=4A_{cs}/L_{cir})$, where $A_{cs}$ is cross sectional area and $L_{cir}$ is circumference of the channel, is needed. Thus,

$$d_h = \frac{4 \cdot (1 \cdot 10^{-3} \times 0.3 \cdot 10^{-3})}{2 \cdot (1 \cdot 10^{-3} + 0.3 \cdot 10^{-3})} = 4.6 \cdot 10^{-4}\,\mathrm{m}$$

$$k_L = \frac{Sh_L D_m}{d_h} = \frac{2.7 \times 1.98 \cdot 10^{-9}}{4.6 \cdot 10^{-4}} = 1.16 \cdot 10^{-5}\,\mathrm{m \cdot s^{-1}}$$

Mass transfer in falling film has been considered mainly with the dependence of liquid-side mass transfer. Recent research activities are concentrated on the potential increase of mass transfer in the liquid film to enhance the reactor performance. For this purpose, different modifications of the surface structure of the reaction plates are proposed.

One way to structure the surface is to mimic a regular porous network. Rhombic structures are used to modify and disturb the laminar liquid flow [52]. So-called "streamlined fins" are arranged horizontally in different rows (Figure 7.14a). The rows are shifted in such a way that one rhombus is positioned in the center of the space between two neighbored rhomb of the up- and downstream rows. This arrangement forces the redirection of the flow, thus ameliorating the mixing of the fluid in a split and recombine manner.

Intensification of liquid mass transfer can also be achieved by structuring the channels of falling film plates in the form of staggered grooves in herring bone arrangements (Figure 7.14b) [52, 53] as presented in Section 4.4.1. This kind of chaotic mixers are very efficient at low Reynolds numbers and allow, in addition, to narrow the residence time distribution of laminar flow (Section 3.6.2).

### 7.4.4 Mass Transfer in Liquid–Liquid Microstructured Devices

#### 7.4.4.1 Slug Flow (Taylor Flow)

The literature on mass transfer in liquid–liquid slug flow is presented in Table 7.7. The mass transfer is investigated for both reacting and nonreacting systems. Most of the results show that the mass transfer coefficient increases with increasing flow velocity.

Identical to gas–liquid Taylor flow, the mass transfer in liquid–liquid slug flow has two contributions: film and slug caps. The specific interfacial area, ratio of surface area of the slug per unit its volume, can be written by neglecting the film thickness as

$$\begin{aligned} a &= a_{cap} + a_{film} \\ &\cong \frac{2 \cdot d_t^2}{d_t^2 \cdot L_b} + \frac{4 \cdot d_t \cdot L_b}{d_t^2 \cdot L_b} = \frac{2}{L_b} + \frac{4}{d_t} \end{aligned} \tag{7.34}$$

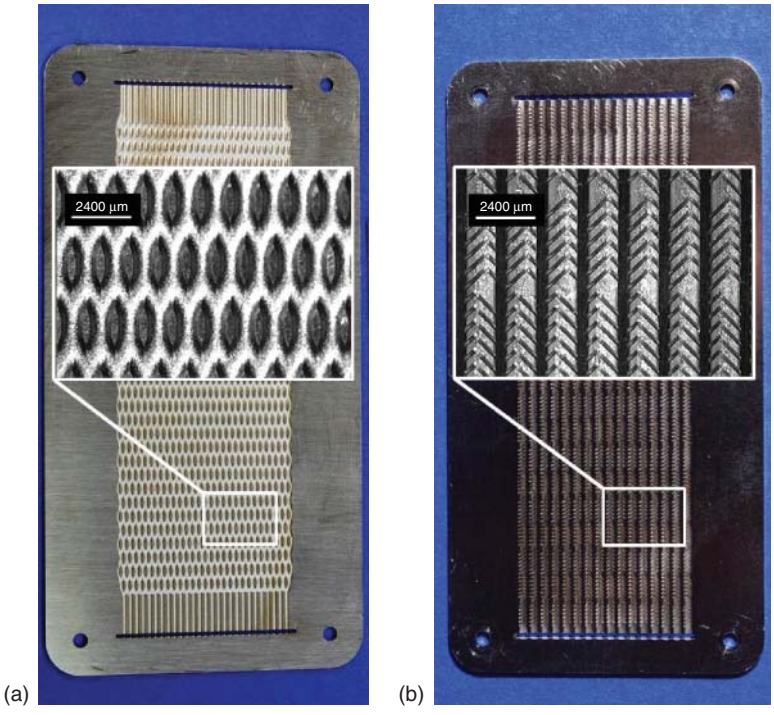


(a) (b)

**Figure 7.14** Photograph of the microstructured falling film plates [52]. Insets show the structure in detail. (a) Reaction plate with rhomb structure. (b) Reaction plate with herring bone structure. Courtesy Fraunhofer ICT-IMM, Germany

where $L_b$ is the length of the dispersed liquid slug. In the case of mass transfer without chemical reaction, the wall film could be saturated and only $a_{\mathrm{cap}}$ $(=2/L_{\mathrm{b}})$ is utilized for mass transfer. In this case, the volumetric mass transfer coefficient is inversely proportional to the slug length in the capillary.

#### 7.4.4.2 Slug-Drop and Deformed Interface Flow

The mass transfer performance of slug-drop and deformed interface flow is given in Table 7.8. The velocity range in the table shows that this flow regime acts as a transition between slug flow and deformed interface flow. When these $k_{\mathrm{ov}}a$ values are compared with those obtained in slug flow regime in an identical microchannel (Table 7.7), the slug-drop shows relatively high values because of larger specific interfacial area formed by small droplets besides regular slugs.

#### 7.4.4.3 Annular and Parallel Flow

The mass transfer coefficients investigated for annular and parallel flow are depicted in Table 7.9. As explained in the flow regime section, this flow exists over a wide range of flow velocities giving $k_{\mathrm{ov}}a$ from 0.07 to 17.35 $\mathrm{s}^{-1}$.

**Table 7.7** Literature review on mass transfer in liquid–liquid slug flow MSR.

| Regime and system | Conditions | Volumetric mass transfer coefficient |
|---|---|---|
| Burns and Ramshaw [35] | | |
| Glass chip reactor<br>Reacting system<br>Kerosene/acetic acid/water + NaOH | $d_h = 380\,\mu m$<br>$C_{\text{acetic acid,or}} = 0.65\,mol \cdot l^{-1}$<br>$C_{NaOH,aq} = 0.1-0.4\,mol \cdot l^{-1}$<br>$u \leq 35\,mm \cdot s^{-1}$ | $k_{ov}a = 0.5\,s^{-1}$<br>Order of magnitude |
| Kashid *et al.* [54] | | |
| Teflon® Y-junction and capillary tubing<br>Nonreacting system<br>Kerosene/acetic acid/water | $d_t = 0.5-1\,mm$<br>$L = 100\,mm$<br>$c_{\text{acetic acid,or}} = 0.03\,mol \cdot l^{-1}$<br>$u = 10-70\,mm \cdot s^{-1}$ | $d_t = 0.5\,mm$ :<br>$k_{ov}a = 0.4-1.4\,s^{-1}$<br>$d_t = 0.75\,mm$ :<br>$k_{ov}a = 0.4-1.1\,s^{-1}$<br>$d_t = 1\,mm$ :<br>$k_{ov}a = 0.4-1\,s^{-1}$ |
| Dessimoz *et al.* [36] | | |
| T and Y-junction glass chip reactor<br>Reacting system<br>Hexane/trichloroacetic acid/water + NaOH | $d_h = 400\,\mu m$<br>$L = 56\,mm$<br>$C_{\text{acid,or}} = 0.6\,mol \cdot l^{-1}$<br>$C_{NaOH,aq} = 0.15-0.3\,mol \cdot l^{-1}$<br>$u \leq 20\,mm \cdot s^{-1}$ | $k_{ov}a = 0.2-0.5\,s^{-1}$ |
| Kashid *et al.* [55] | | |
| T-junction/square channel<br>Nonreacting system<br>Water-acetone-toluene | TS : $d_h = 400\,\mu m$ $L =$ $56\,mm$, $u = 0.1-0.42\,m \cdot s^{-1}$<br>$c_{\text{acetone,aq}} = 3.5\,wt\%$ | $k_{ov}a = 0.11-0.74\,s^{-1}$ |

**Table 7.8** Mass transfer literature on slug-drop and deformed interface flow.

| Regime and system[a)] | Conditions[a)] | Volumetric mass transfer coefficient |
|---|---|---|
| Slug-drop flow | $u = 0.42\,m \cdot s^{-1}$ | $k_{ov}a = 0.47\,s^{-1}$ |
| Deformed interface flow | $u = 0.63-1.04\,m \cdot s^{-1}$ | $k_{ov}a = 0.66-1.05\,s^{-1}$ |

a) T-junction/square channel, *Nonreacting system: water-acetone-toluene.*
Source: Adapted from Ref. [55].

#### 7.4.4.4 Slug-Dispersed and Dispersed Flow

The mass transfer performance of a caterpillar micromixer under slug-dispersed flow regime is given in Table 7.10. The fine dispersion results in very high specific interfacial area leading to $k_{ov}a$ as high as $2.25\,s^{-1}$.

Unlike for gas–liquid systems, no efforts have been made to develop mass transfer models based on either film or penetration theory for liquid–liquid MSR. The

**Table 7.9** Mass transfer literature data on annular and parallel flow.

| Regime and system | Conditions | Volumetric mass transfer coefficient |
|---|---|---|
| Zhao *et al.* [56] | | |
| Annular/parallel flow | $L = 45, 60\,\text{mm}$ | $k_{ov}a = 0.067 - 17.35\,\text{s}^{-1}$ |
| Nonreacting system | $d_h = 0.4\,\text{mm}, u = 0.01 - 2.5\,\text{mm} \cdot \text{s}^{-1}$ | |
| Water-succinic | $d_h = 0.6\,\text{mm}, u = 0.005 - 2\,\text{mm} \cdot \text{s}^{-1}$ | |
| acid-*n*-butanol | $c_{\text{acid,or}} = 1\,\text{wt\%}$ | |
| Dessimoz *et al.* [36] | | |
| T and Y-junction glass | $d_h = 269\,\mu\text{m}$ | $k_{ov}a = 0.2 - 0.5\,\text{s}^{-1}$ |
| chip reactor | $L = 40\,\text{mm}$ | |
| Parallel flow | $c_{\text{acid,or}} = 0.6\,\text{mol} \cdot \text{l}^{-1}$ | |
| Reacting system | $c_{\text{NaOH,aq}} = 0.1 - 0.2\,\text{mol} \cdot \text{l}^{-1}$ | |
| Toluene/trichloroacetic | $u = 0 - 50\,\text{mm} \cdot \text{s}^{-1}$ | |
| acid/water + NaOH | | |
| Kashid *et al.* [55] | | |
| Parallel flow | $u = 1.25 - 1.88\,\text{m} \cdot \text{s}^{-1}$ | $k_{ov}a = 1.12 - 1.27\,\text{s}^{-1}$ |
| T-junction/square channel | | |
| Nonreacting system | | |
| Water-acetone-toluene | | |

**Table 7.10** Mass transfer literature on slug-dispersed and dispersed flow.

| Regime and system[a)] | Conditions[a)] | Volumetric mass transfer coefficient |
|---|---|---|
| Slug-dispersed flow | $u = 5.92 - 8.88\,\text{m} \cdot \text{s}^{-1}$ | $k_{ov}a = 1 - 1.5\,\text{s}^{-1}$ |
| Dispersed flow | $u = 10.37 - 13.33\,\text{m} \cdot \text{s}^{-1}$ | $k_{ov}a = 1.61 - 2.25\,\text{s}^{-1}$ |

a) Concentric-junction/circular channel, *Nonreacting system: water-acetone-toluene.*
Source: Adapted from Ref. [55].

complexity in the liquid–liquid systems is because of the resistance on both liquid phases, whereas in gas–liquid systems the main resistance to mass transfer is mostly in the liquid phase.

### 7.4.5 Comparison with Conventional Contactors

The mass transfer coefficients obtained in microstructured devices and in conventional gas–liquid contactors are listed in Table 7.11. The liquid-side $k_L a$ and interfacial area in microstructured devices are at least 1 order of magnitude higher than those in conventional contactors such as bubble columns and packed columns, being up to $21\,\text{s}^{-1}$.

**Table 7.11** Comparison of gas–liquid microstructured devices with conventional contactors.

| Type of contactor | $k_L \times 10^5$ (m s$^{-1}$) | $a$ (m$^2$ m$^{-3}$) | $k_L a$ (s$^{-1}$) |
|---|---|---|---|
| Bubble columns | 10–40 | 50–600 | 0.005–0.24 |
| Couette–Taylor flow reactor | 9–20 | 200–1200 | 0.03–0.21 |
| Impinging jet absorbers | 29–66 | 90–2050 | 0.025–1.22 |
| Packed columns, concurrent | 4–60 | 10–1700 | 0.0004–1.02 |
| Packed columns, countercurrent | 4–20 | 10–350 | 0.0004–0.07 |
| Spray column | 12–19 | 75–170 | 0.015–0.022 |
| Static mixers | 100–450 | 100–1000 | 0.1–2.5 |
| Stirred tank | 0.3–80 | 100–2000 | 0.03–0.4 |
| Tube reactors, horizontal, and coiled | 10–100 | 50–700 | 0.005–0.7 |
| Tube reactors, vertical | 20–50 | 100–2000 | 0.02–1 |
| Gas–liquid microchannel | 40–160 | 3400–9000 | 0.3–21 |

Source: Adapted from Yue *et al.* [32].

**Table 7.12** Comparison of liquid–liquid microstructured devices with conventional equipment.

| Contactor | $a$ (m$^2$ m$^{-3}$) | $k_{ov}a$ (s$^{-1}$) |
|---|---|---|
| Agitated contactor [57] | 32–311 | 0.048–0.083 |
| Packed bed column (Pall/Raschig ring, Intalox saddles) [58] | 80–450 | 0.0034–0.005 |
| RTL extractor (Graesser raining bucket) [59] | 90–140 | 0.0006–0.0013 |
| Air operated two impinging jet reactors [60] | 350–900 | 0.075 |
| Two impinging jets reactor [61] | 1000–3400 | 0.28 |
| Capillary microchannel (ID = 0.5–1 mm) | 830–3200 | 0.88–1.67 |

The volumetric mass transfer coefficients found in the liquid–liquid microstructured devices at various flow rates were compared with those for conventional equipment in Table 7.12. Identical to gas–liquid devices, the mass transfer coefficients found in liquid–liquid microstructured devices are well above those of conventional contactors.

## 7.5 Pressure Drop in Fluid–Fluid Microstructured Channels

Besides the mass transfer coefficient, pressure drop plays an important role in the design of microstructured devices. The discussion here is focused on Taylor flow and annular flow.

### 7.5.1 Pressure Drop in Gas–Liquid Flow

Two models can be proposed [62]:

1) the homogenous model with mean flow velocity similar to single-phase flow, and
2) the separated flow model with an artificially separated gas and liquid flow.

Model (1): One of the most commonly used models to characterize the pressure drop in microchannels is that proposed by Lockhart and Martinelli [63] for *gas–liquid horizontal flow* in pipes, which is used for all regimes. It employs two friction multipliers for gas and liquid, $\Phi_G^2$ and $\Phi_L^2$, as given by the following equation:

$$\left(\frac{\Delta p_f}{L}\right)_{2p} = \Phi_G^2 \left(\frac{\Delta p_f}{L}\right)_G \tag{7.35}$$

or

$$\left(\frac{\Delta p_f}{L}\right)_{2p} = \Phi_L^2 \left(\frac{\Delta p_f}{L}\right)_L \tag{7.36}$$

where the index $2p$ indicates two-phase flow.

The two equations given above are correlated in terms of a dimensionless number called the *Lockhart–Martinelli parameter* ($\Psi$). It is the ratio of the single-phase pressure drop of liquid to that of the gas and given by

$$\Psi = \frac{\left(\frac{\Delta p_f}{L}\right)_L}{\left(\frac{\Delta p_f}{L}\right)_G} \tag{7.37}$$

Here $(\Delta p_f/L)_L$ and $(\Delta p_f/L)_G$ are the frictional pressure drop gradients when liquid and gas are assumed to flow in the microchannel alone, respectively. They are calculated as

$$\begin{aligned}
\left(\frac{\Delta p_f}{L}\right)_L &= \frac{2 f_L \dot{m}_{\text{total}}^2 (1 - x_G)^2}{d_h \rho_L} \\
\left(\frac{\Delta p_f}{L}\right)_G &= \frac{2 f_G \dot{m}_{\text{total}}^2 x_G^2}{A_{CS} d_h \rho_G} \\
x_G &= \frac{\dot{m}_G}{\dot{m}_G + \dot{m}_L} = \frac{\dot{m}_G}{\dot{m}_{\text{total}}}
\end{aligned} \tag{7.38}$$

The liquid friction factor $f_L$ and liquid Reynolds number (and vapor friction factor $f_G$ and gas Reynolds number with the gas viscosity) are obtained from

$$f_i = \frac{0.079}{Re_i^{0.25}}; Re_i = \frac{\dot{m}_{\text{total}} d_h}{A_{CS} \mu_i} \tag{7.39}$$

The relationship between $\Phi_L^2$ and $\Psi$ can be obtained from the widely used Chisholm's equation [64]:

$$\Phi_L^2 = 1 + \frac{C}{\Psi} + \frac{1}{\Psi^2} \tag{7.40}$$

where $C$ is a constant, ranging from 5 to 20, depending on the flow pattern of gas and liquid in the channel. In the case of microchannels, the Reynolds number for both the liquid and gas phases are less than 1000 and the constant $C$ is considered to be about 5 [64]. However, from experimental measurements [32], it is reported for the $CO_2$-water system in rectangular microchannels that the friction multiplier cannot be predicted reliably with a single value of $C$. It was found to become greater with increasing mass flux and, therefore, a new correlation was proposed with a standard deviation of 9.2%:

$$C = 0.185\Psi^{-0.0942}Re^{0.711} \tag{7.41}$$

Thus, the steps in estimating the pressure drop using Equation 7.36 are: (i) estimation of the frictional pressure drop of each individual phase, (ii) calculation of the Lockhart–Martinelli parameter ($\Psi$), and (iii) estimation of the friction multiplier for liquid, and $\Phi_L^2$.

Model (2): A flow-regime-dependent relationship for estimating the total pressure drop in a two-phase *vertical capillary flows* was reported [16]. Initially a single-phase vertical tube with liquid flowing in the laminar regime was considered. The total pressure drop ($\Delta p_{\text{tot}}$) is composed of two contributions: (i) the pressure drop because of frictional effects of the liquid flow ($\Delta p_f$) and (ii) the hydrostatic pressure of the liquid:

$$\Delta p_{\text{tot}} = \Delta p_f + \rho_L g \cdot L \tag{7.42}$$

For laminar flow, the frictional pressure drop is given by the Hagen–Poiseuille equation

$$\Delta p_f = \frac{32\mu_L u_L L}{d_t^2} \tag{7.43}$$

Combining both equations, the total pressure drop is given by:

$$\Delta p_{\text{tot}} = \frac{32\mu_L L}{d_t^2}\left[u_L + \left(\frac{d_t^2}{32\mu_L}\right)\rho_L g\right] \tag{7.44}$$

By comparing Equations 7.43 and 7.44 a gravity equivalent liquid velocity ($u_g$) in the capillary can be introduced that would result in a pressure loss equal to the hydrostatic pressure exerted by the liquid phase. Assuming laminar flow, the gravity equivalent liquid velocity becomes:

$$u_g = \left(\frac{d_t^2}{32\mu_L}\right)(1 - \varepsilon_G)\rho_L g \tag{7.45}$$

The gas hold-up $\varepsilon_G$ in the capillary can be estimated with Equations 7.4 and 7.5:

The total mixture velocity ($u_{tot}$) is defined as the sum of the superficial velocities of the two phases and the gravity equivalent velocity ($u_g$):

$$u_{tot} = u_G + u_L + u_g \tag{7.46}$$

A dimensionless two-phase pressure factor $f_{tot}$ can be defined, analogous to the Fanning friction factor [65]:

$$f_{tot} = \frac{\Delta p_{tot}/L}{1/2\rho_L u_{tot}^2 (4/d_t)} \tag{7.47}$$

In a situation where both the gas- and liquid phase flows are laminar, the pressure factor can be expected similarly to the Fanning friction factor as:

$$f_{tot} = \frac{C}{Re_{tot}} \text{ with } Re_{tot} = \frac{\rho_L u_{tot} d_t}{\mu_L} \tag{7.48}$$

The constant $C$ depends on the channel geometry and has values of 16 and 14.2 for circular and square channels, respectively.

For $u_G/u_L < 0.5$ the pressure factor can be estimated with Equation 7.48. At $u_G/u_L > 0.5$ and $u_G/(u_G + u_L) < 0.5$ the slip ratio $R_{slip}$ between bubble and liquid velocity influences the friction factor:

$$R_{slip} = \frac{u_G/\varepsilon_G}{u_L/(1-\varepsilon_G)} \tag{7.49}$$

To predict the pressure drop for this flow regime, an empirical correlation for estimating the friction factor was obtained from experimental data in the range of $0.008 < (u_G + u_L) < 1\ \text{ms}^{-1}$:

$$f_{tot} = \frac{C}{Re_{tot}} \frac{1}{\sqrt{R_{slip}}} \left[\exp\left(-0.02 Re_{tot}\right) + 0.07 Re_{tot}^{0.34}\right] \tag{7.50}$$

The pressure drop results using above equation are demonstrated in Example 7.5.

**Example 7.5: Pressure drop in upward gas-liquid flow in a circular capillary**

Estimate the pressure drop in upward gas–liquid flow in a circular capillary for air–water system as a function of gas flow velocity (range $1-30\ \text{mm s}^{-1}$) for different liquid flow velocities of 30, 50, and $75\ \text{mm s}^{-1}$. The hydraulic of the channel is 2 mm.

***Solution:***

The pressure drop in upward gas–liquid flow in a square capillary is investigated using Equation 7.47.

$$\frac{\Delta p_{tot}}{L} = f_{tot} \frac{1}{2} \rho_L u_{tot}^2 \left(\frac{4}{d_t}\right) \tag{7.51}$$

The friction factor is approximated with Equation 7.50.

The pressure drop as a function of the superficial gas velocity is plotted in Figure 7.15.

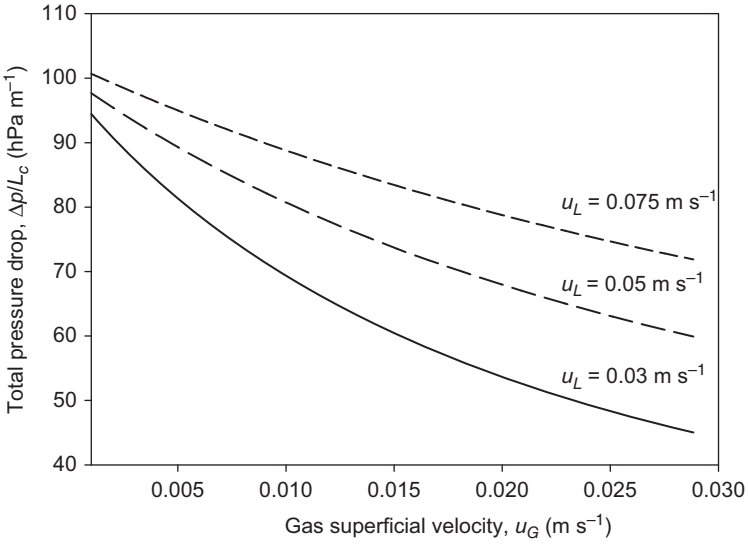


**Figure 7.15** Pressure drop in upward gas–liquid flow in a circular capillary of $d_h = 2$ mm.

### 7.5.2
### Pressure Drop in Liquid–Liquid Flow

There are two fundamental differences between gas–liquid and liquid–liquid slug flow in microchannels [37].

- In the liquid–liquid slug flow system, because of close physical properties of both fluids it might be possible that there is no wall film and both fluids flow alternatively through the capillary; this is not observed in gas–liquid systems.
- In the case of a wall film in the horizontal microchannel, because of considerable shear of the discrete liquid phase on the continuous phase, the latter moves with finite velocity while film in the gas–liquid system is considered stagnant.

#### 7.5.2.1 Pressure Drop – Without Film

In the case of *without film,* the pressure drop in liquid–liquid slug flow comes from two main contributions: the hydrodynamic pressure drop of the individual phases and the pressure drop because of capillary phenomena, $p_c$. If we consider the single flow unit shown in Figure 7.16a, the overall pressure drop along its length can be written as:

$$\Delta p_{\text{tot}} = \Delta p_1 + \Delta p_2 + p_C \tag{7.52}$$

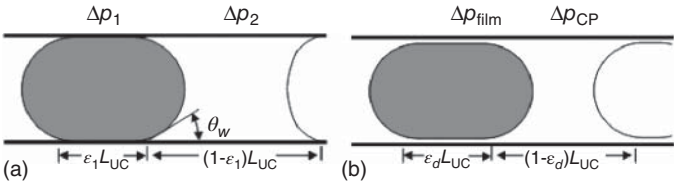


**Figure 7.16** Pressure drop along a single slug unit. (a) Without film and (b) with film.

The single-phase hydrodynamic pressure drop can be calculated using the Hagen–Poiseuille equation, while the capillary pressure is obtained from the Young–Laplace equation for a cylindrical tube as given by the following equations:

$$\Delta p_1 = \frac{32\mu_1 u \varepsilon_1 L_{UC}}{d_t^2}; \Delta p_2 = \frac{32\mu_2 u(1-\varepsilon_1)L_{UC}}{d_t^2} \text{ and } p_c = \frac{4\sigma}{d_t}\cos\theta_w$$
$$\text{where, } u = \frac{\dot{V}_1 + \dot{V}_2}{A_{cs}}, \varepsilon_1 = \frac{\dot{V}_1}{\dot{V}_1 + \dot{V}_2} \tag{7.53}$$

Here $A_{cs}$ is the cross sectional area of the circular channel. Assuming a constant dynamic contact angle and slug lengths with an equal number of slugs of both phases under similar operating conditions and neglecting end effects, the overall pressure across for a given length of the capillary is the summation of pressure drops across all slugs and the capillary pressure at all interfaces.

#### 7.5.2.2 Pressure Drop – With Film

For theoretical predictions, it is assumed that the pressure drop along the length of the capillary is because of the film region only. A model for pressure drop in the pipeline flow of slugs (referred to as "*capsules*") is given by Charles [66], which relates the pressure drop in the slug region, $(\Delta p/L)_{film}$, to that of single-phase flow of the continuous phase, $(\Delta p/L)_{CP}$. According to this model, the pressure drop along the length of the film can be determined by the following equation:

$$\left(\frac{\Delta p}{L}\right)_{film} = \left(\frac{1}{1-\kappa^4}\right)\left(\frac{\Delta p}{L}\right)_{CP}; \kappa = \frac{R-\delta_{film}}{R}; R = \frac{d_t}{2} \tag{7.54}$$

where $L$ and $R$ is length and radius of the tube, respectively. In the above model, it was assumed that slugs follow each other sufficiently closely so that the fluid between them can be considered as part of the slug stream. However, in the liquid–liquid slug flow for chemical engineering applications, this assumption is usually not valid and will apply only when the enclosed slug has a length of several times more than the other slug. The slug that forms the film may, however, be longer depending on the inlet flow ratio for both phases. It is, therefore, necessary to consider the phase fraction of both liquids to calculate the pressure drop for a given length of the liquid–liquid slug flow microchannel. In addition, the film thickness is very small compared to the radius of the slug, which justifies

the assumption that the length of the film region for a given length of capillary is nothing more than the corresponding phase fraction times the total length. Assuming phase fraction inside the capillary equal to volumetric flow fraction (for dispersed phase, $\varepsilon_D$), the pressure drop along the film region for a given pipe length can thus be written as [37]:

$$\frac{\Delta p}{L} = \left(\frac{\Delta p}{L}\right)_{\text{film}} = \left(\frac{\varepsilon_D}{1-\kappa^4}\right)\left(\frac{\Delta p}{L}\right)_{\text{CP}}$$
$$\text{with } \varepsilon_D, \text{the volume fraction of the dispersed phase} \tag{7.55}$$

To calculate the pressure drop using the above equation, the film thickness is crucial. It can be estimated using Bretherton's or Aussillon and Quere's correlations depending on the capillary number (Equations 7.2 or 7.3) as demonstrated in Example 7.6.

**Example 7.6: Pressure drop in liquid-liquid slug flow**

A liquid–liquid system flows in a circular cross section capillary with $d_t = 0.8\,\text{mm}$ diameter forming a continuous water phase and a dispersed toluene phase. The flow rate of the continuous phase is $5\,\text{ml}\,\text{min}^{-1}$ while the flow rate of the dispersed phase is $4\,\text{ml}\,\text{min}^{-1}$. Estimate the pressure drop in the microchannel assuming dispersed slug velocity equals the two-phase velocity.

**Data:** $\rho_{\text{toluene}} = \rho_D = 867\,\text{kg}\cdot\text{m}^{-3}$, $\mu_{\text{toluene}} = \mu_D = 0.6\cdot10^{-3}\,\text{Pa s}$, $\rho_{\text{water}} = \rho_C = 998.2\,\text{kg}\cdot\text{m}^{-3}$, $\mu_{\text{water}} = \mu_C = 1\cdot10^{-3}\,\text{Pa s}$, $\sigma = 0.036\,\text{N}\,\text{m}^{-1}$.

***Solution:***

As the two-phase systems form dispersed and continuous phase, Equation 7.53 can be used. It requires single-phase pressure drop and $\kappa$. The single-phase pressure drop can be calculated using Hagen–Poisseuille equation (Equation 7.42).

$$\left(\frac{\Delta p}{L}\right)_{\text{CP}} = 32\frac{\mu_C u}{d_t^2} = 128\frac{\mu_C \dot{V}}{\pi d_t^4} \text{for circular channels}$$

The single phase pressure drop of the continuous phase is calculated with the velocity of the two-phase system ($u = u_D + u_C$) or flow rate two phases.

$$\left(\frac{\Delta p}{L}\right)_{\text{CP}} = 128\frac{\mu_C \dot{V}}{\pi d_t^4}$$
$$= 128\cdot\frac{1\cdot10^{-3}\cdot\left(\frac{5+4}{60}\cdot10^{-6}\right)}{\pi\cdot(0.8\cdot10^{-3})^4} = 14920\,\text{Pa}\cdot\text{m}^{-1}$$

To determine the film thickness the capillary number must be known:

$$Ca_i = \frac{\mu_i \cdot u_b}{\sigma} \tag{7.1}$$

Here the bubble velocity corresponds to the velocity of the slug of the dispersed flow, which was assumed to be identical with the twophase flow velocity ($u_b = u_{D,\text{slug}} \cong u$).

$$u = \frac{\dot{V}}{\frac{\pi}{4} d_h^2} = \frac{\left(\frac{5+4}{60} \times 10^{-6}\right)}{\frac{\pi}{4} \times (0.8 \cdot 10^{-3})^2} = 0.30\,\text{m} \cdot \text{s}^{-1}$$

$$Ca_C = \frac{\mu_C \cdot u}{\sigma} = \frac{10^{-3} \cdot 0.3}{0.036} = 8.3 \cdot 10^{-3}$$

For capillary number greater than $3 \cdot 10^{-3}$ the relation of Aussillons and Quere is used to estimate the film thickness (Equation 7.3):

$$\delta_{\text{film}} = d_t \frac{0.67 Ca_C^{2/3}}{1 + 3.35 Ca_C^{2/3}} = 0.8 \cdot 10^{-3} \frac{0.67 \cdot (8.3 \cdot 10^{-3})^{2/3}}{1 + 3.35 \cdot (8.3 \cdot 10^{-3})^{2/3}} = 1.93 \cdot 10^{-5}\,\text{m}$$

The value of $\kappa$ is found to be $\kappa = \frac{R - \delta_{\text{film}}}{R} = \frac{0.4 \cdot 10^{-3} - 1.94 \cdot 10^{-5}}{0.4 \cdot 10^{-3}} = 0.9515$
Thus, the two-phase pressure drop can be determined with Equation 7.55:

$$\frac{\Delta p}{L} = \left(\frac{\varepsilon_D}{1 - \kappa^4}\right)\left(\frac{\Delta p}{L}\right)_{\text{CP}} = \left(\frac{\frac{4}{5+4}}{1 - (0.9515)^4}\right) \times 14920$$
$$= 3.67 \cdot 10^4\,\text{Pa} \cdot \text{m}^{-1} = 0.367\,\text{bar} \cdot \text{m}^{-1}$$

#### 7.5.2.3 Power Dissipation in Liquid/Liquid Reactors

Power input, a decisive parameter for benchmarking technical reactors, has been investigated using the experimental pressure drop and compared with conventional contactor as shown in Table 7.13. The power input for continuous reactors is investigated in terms of kJ $m^{-3}$ of liquid, product of pressure drop and volumetric flow rate. The comparison reveals that the liquid–liquid slug flow microreactor requires much less power than the alternatives to provide large interfacial area – as high as $a = 5000\,\text{m}^2\,\text{m}^{-3}$ in 0.5 mm capillary microreactor, which is above the values in a mechanically agitated reactor ($a \approx 500\,\text{m}^2\,\text{m}^{-3}$). The specific interfacial area obtained for conventional liquid contactor is summarized in Table 7.12.

## 7.6 Flow Separation in Liquid–Liquid Microstructured Reactors

The separation of dissolved components by liquid–liquid extraction has been discussed in the mass transfer section. In this section, flow separators required for splitting biphasic mixture are presented.

**Table 7.13** Power input requirement for various liquid–liquid contactors [67].

| Contactor type | Power input, (kJ $m^{-3}$) of liquid |
|---|---|
| Agitated extraction column | 0.5–190 |
| Mixer-settler | 150–250 |
| Rotating disk impinging streams contactor | 175–250 |
| Impinging streams | 280 |
| Impinging stream extractor | 35–1500 |
| Centrifugal extractor | 850–2600 |
| Liquid–liquid slug flow | 0.2–20 |

### 7.6.1 Conventional Separators

Separation of two liquid phases after the mass transfer is an important step in the liquid–liquid extraction. Therefore, when designing an extraction unit, a question always arises as how to achieve the separation of two phases immediately following phase contact in the extraction zone. In conventional extraction equipment, the operations associated with mixing and separation of two liquids is usually at least partially distinct.

Gravity based separation, dependent on the density difference between two phases, is the most commonly used method of separation. Difficulties that often occur in the separation of immiscible liquids include poor or slow phase separation, emulsion or rag layer formation, and poor process control, especially in batch systems. Some liquid–liquid dispersions take hours to separate in conventional systems resulting in poor performances of the extraction units.

In addition to the single-stage operation, as discussed above, multistage operations are common in liquid–liquid extraction for large-scale production and effective use of chemicals. Depending on the selectivity of the solvent and the amount of mass transfer required to achieve the desired solute recovery, several stages of extraction may be required. In this case, countercurrent contact is the most efficient extraction method as it conserves the mass transfer driving force and, therefore, gives optimal performance. Most of the countercurrent operations in the laboratory practice use batch processes and they are carried out using milliliter amount of feed and solvent in the flasks.

### 7.6.2 Types of Microstructured Separators

Flow separation after the mass transfer zone in microstructured devices has been a topic of research for a long time.

The schematics of the phase separators used for liquid–liquid separation are depicted in Figure 7.17. Three principles are used: geometrical modifications, wettability based separation, and gravity based separators. These are discussed in the following section.

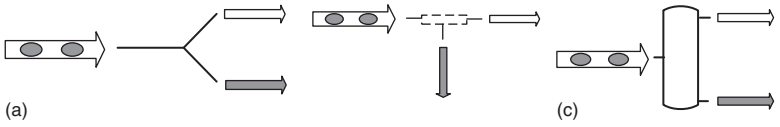


**Figure 7.17** Schematics of different types of flow splitters for separation of liquid–liquid two-phase flow. (a) Geometrical modifications (e.g., Y-separator), (b) wettability based (e.g., membrane separator), and (c) gravity based separator (e.g., settler).

#### 7.6.2.1 Geometrical Modifications

In this case, either geometry or liquid properties are modified or selected to generate the parallel flow of two liquids. The surface tension forces pinning the liquid to the channel walls are generally strong enough to resist buoyancy and viscous shear forces. In such cases, it is also possible that lighter liquid may flow under the denser fluid. The pressure drop in each outlet can be calculated using Hagen–Poiseuille equation in terms of flow ratio:

$$\Delta p_{\text{out}} = 32\zeta \frac{\mu u}{d_h^2} L = 128\zeta \frac{\mu \dot{V} L}{\pi d_h^4} \tag{7.56}$$

where $\zeta$ is a geometric factor, which is 1 for a circular tube and it depends on the height ($H$) to width ($W$) ratio for a rectangular channel. Here L refers to the length of separator outlets. The correction factor becomes 0.89 for quadratic channels and assumes the asymptotic value 1.5 when the ratio goes to zero. An empirical correlation is given by the following expression [68]:

$$\zeta = 0.8735 + 0.6265 \exp\left(-3.636 \frac{H}{W}\right) \tag{7.57}$$

Ideally, the pressure drop in each outlet should be equal along each outlet ($\Delta p_{\text{out}}$) with only one phase per outlet [69]:

$$\Delta p_{\text{out}} = \mu_1 \dot{V}_1 \left(\frac{128\zeta L}{\pi d_h^4}\right)_1 = \mu_2 \dot{V}_2 \left(\frac{128\zeta L}{\pi d_h^4}\right)_2 \tag{7.58}$$

and the flow ratio $S$ for ideal splitting can be calculated:

$$S = \frac{\dot{V}_2}{\dot{V}_1} = \frac{\mu_1}{\mu_2} \frac{(128\zeta L/d_h^4)_1}{(128\zeta L/d_h^4)_2} \tag{7.59}$$

The characterization of the splitter is done in terms of contamination ($C'$) in each outlet of the splitter:

$$C' = \frac{\text{Volume of undesired sample}}{\text{Total volume collected}} \tag{7.60}$$

And the average contamination ($C'_{\text{av}}$) in two outlets is investigated by following equation:

$$C'_{\text{av}} = \frac{1}{2}\left[\frac{V_{1,2}}{V_{1,2} + V_{2,2}} + \frac{V_{2,1}}{V_{1,1} + V_{2,1}}\right] \tag{7.61}$$

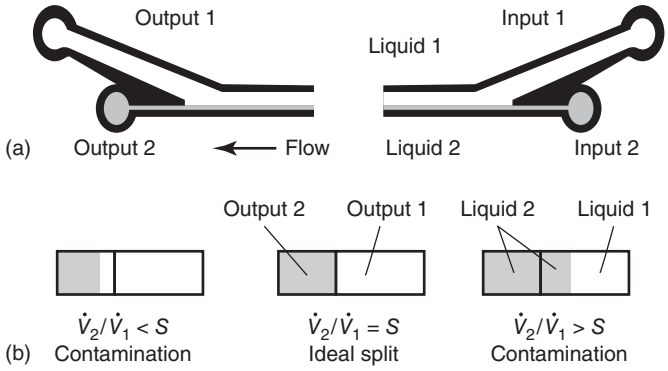


**Figure 7.18** A wedge-shaped flow splitter to split parallel flow. (a) Inlets and outlets of wedge shapes separator and (b) schematic presentation of contamination and ideal split [69]. (Adapted with permission from Elsevier.)

where $V$ is the volume collected at the outlet at a certain time. The subscript $i, j$ indicates fluid and outlet numbers, respectively.

A wedge-shaped flow splitter to split parallel flow has already been applied for the separation of the parallel flow of kerosene (+dye) and aqueous solution of propylene glycol as shown in Figure 7.18. In this example, the lighter kerosene phase flowed under the dense aqueous solution. The viscosity of fluids varied by adding propylene glycol to water and it was observed that at low viscosity ratio of 0.56 and 3.06, the flow was stabilized while at higher viscosity ratio of 22.1 disrupted flow patterns were observed. A contamination level below 2% was achieved. By changing the flow ratio, higher or lower, than its ideal value $S$ (Equation 7.59), one outlet could be made contamination free. This may be the preferred mode of operation for many systems as it provides one stable clean output at the expense of slightly higher contamination in the other (Figure 7.18).

#### 7.6.2.2 **Wettability Based Flow Splitters**

Every liquid has an ability to maintain contact with some solid materials, which is often referred to as *wetting*. The degree of wetting is represented in terms of contact angles ($\theta_w$), angle at which the liquid–vapor interface meets the solid–liquid interface, as shown in Figure 7.19a. It indicates that wetting is poor at $\theta_w > 90°$, good at $\theta_w \ll 90°$, and complete at $\theta_w \sim 0°$.

If two materials with preferential wettability of two liquids are considered, the liquids have a tendency to flow along the surface of the material to which they have the greatest affinity. The behavior of drop on the zone-selectively modified with hydrophilic and hydrophobic material is shown in Figure 7.19b. The liquid drop was placed on the boundary of hydrophilic and hydrophobic zones on a plate immersed in another immiscible liquid. In the case of octane drop for the plate immersed in water, it was moved toward the hydrophobic zone and settled and when the two-zone plate was dipped in octane and a water drop was placed on the boundary, and the drop settled in the hydrophilic zone

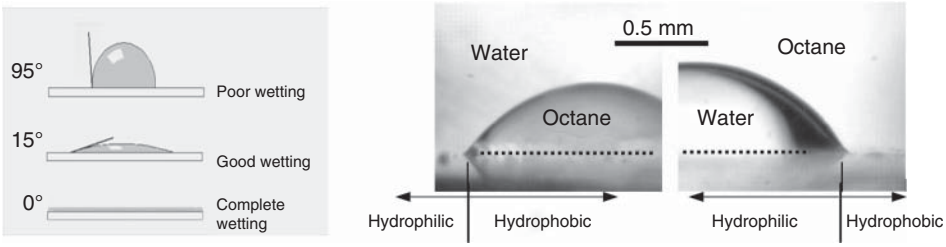


**Figure 7.19** Contact angle [70]. (a) Contact angle and wetting of solids. (b) Behavior of three-phase contact angle when the liquid drop placed on boundary of hydrophilic and hydrophobic material for octane drop on the plate immersed in water and water drop on the plate immersed in octane. (Adapted from Ref. [70]. Copyright © 2013, Wiley-VCH GmbH & Co. KGaA.)

[71]. The photographs suggest that the boundary between water and octane could be pinned along the boundary between the hydrophilic and hydrophobic regions. These preferential displacements can be used to separate two liquid phases.

Different types of wettability based separators have been used for the separation of two immiscible liquids. Some of the examples are shown in Figure 7.20. The Y-shaped separator was used for aqueous-organic systems comprising one inlet and two outlets. The splitter consists of PTFE with a steel needle having an internal diameter equal to the Y-junction, being fitted into one of the outlets. The aqueous phase has a strong affinity toward steel, whereas the organic phase has an affinity toward PTFE. This difference in the affinity can be harnessed for the separation of the two phases. The results show that the average contamination was about 5%. The results show that there is no significant effect of flow rate and capillary size on flow splitting for a given splitter. The minor problems observed with phase cross contamination could be resolved by modifying the splitting geometry.

One of the possible modifications could be the transition of slug flow regime to parallel flow in the beginning of flow splitter. A flow splitter made up of PTFE and stainless steel with rectangular cross section is depicted in Figure 7.21. The slug flow becomes parallel because of rectangular cross section and preferential wettability of the separator enhancing the separation. Further modifications are used in a flow splitter that consists of a set of grooves on two surfaces having different surface properties (e.g., one could be glass and the other an organic material) and fixing those surfaces on to each other to form channels in between them [73]. The experiments performed with a chip consisting of two layers, one coated with polar (glass) and nonpolar (a silicon monomer mix) materials for separating isooctane and water showed excellent results.

The presented technique is suitable for use in microscale equipment, in which surface tension forces, rather than gravitational force, dominate.

The wettability based separation of two immiscible liquids is explained in more detail for the membrane separator [72].

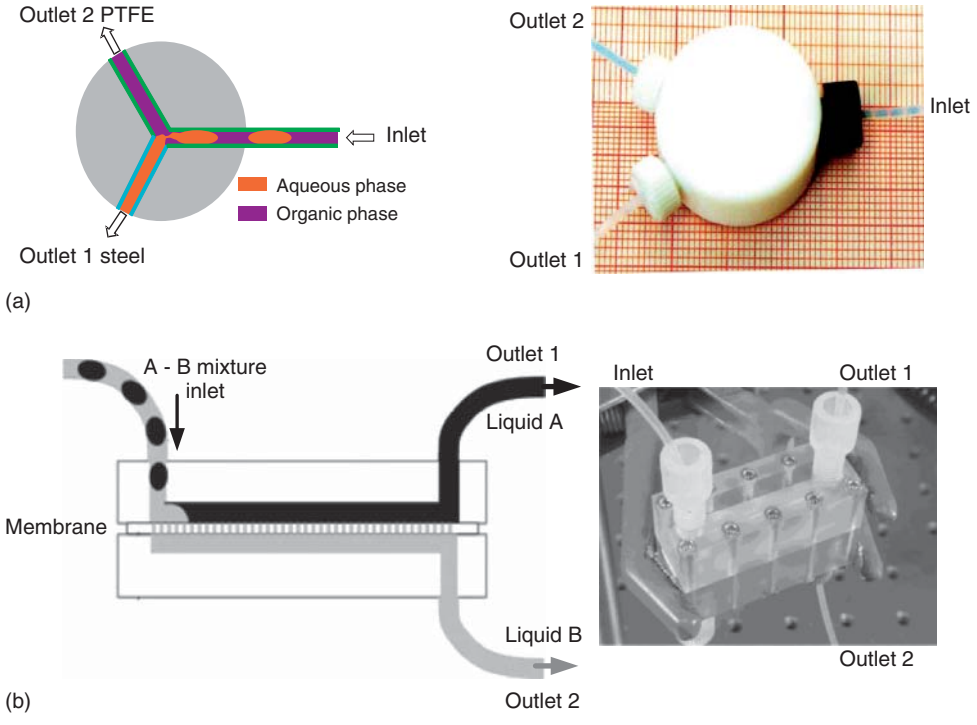


**Figure 7.20** Schematics of wettability based separators. (a) Y-shaped separator. (Adapted with permission from Ref. [54]. Copyright (2007) American Chemical Society.) (b) Membrane separator. (Adapted from Ref. [72] with permission of The Royal Society of Chemistry.)

The pressure drop in the separator outlets should be identical because the two-fluid streams exit at the same ambient pressure (Equation 7.58). However, it is proposed that the design of the microseparator should be based on a worst case criteria where the pressure drop in dispersed phase outlet should be calculated on the total flow rate [72].

In the case of slug flow, the movement of slugs to the nondesired outlet can be restricted with the capillary pressure [72] (Figure 7.20b). The correct design of the membrane separator allows to get noncontaminated liquid flows at outlet 1 and 2. Let us assume a slug flow of an organic liquid (B), for example, hexane, toluene from an aqueous phase (A). The mixture enters the separator equipped with a hydrophobic membrane, for example, PTFE. The aqueous phase leaves the separator at outlet 1 whereas the organic phase, which is wetting the membrane, flows through the pores leaving the device at outlet 2. The maximum pressure drop through outlet 1 is obtained when the whole flow leaves the device at position 1. This is the worst case applied for the design. Using Hagen–Poiseuille relation for laminar flow we obtain:

$$\Delta p_1 = \frac{128 \cdot \mu_1 \cdot \dot{V}_{\text{tot}}}{\pi \cdot d_1^4} L_1; \dot{V}_{\text{tot}} = \dot{V}_1 + \dot{V}_2 \tag{7.62}$$

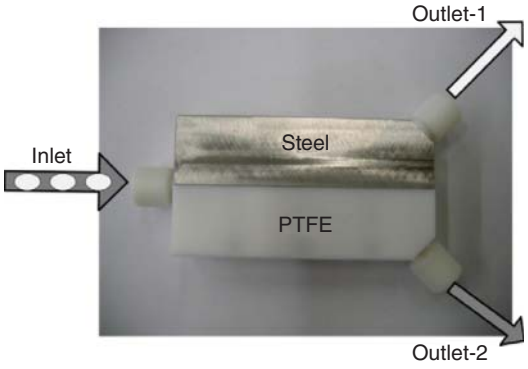


**Figure 7.21** A new flow splitter developed for the separation of biphasic mixture. (Adapted from Ref. [70]. Copyright © 2013, Wiley-VCH GmbH & Co. KGaA.)

with $\mu_1$ the dynamic viscosity of the aqueous phase.

The pressure drop in the channel (connected to membrane) on the aqueous side of the separator devices is given by:

$$\Delta p_{\text{sep}} = \frac{128 \cdot \mu_1 \cdot \dot{V}_{\text{tot}}}{\pi \cdot d_{\text{sep}}^4} L_{\text{sep}} \tag{7.63}$$

In most practical situations the pressure drop in the separator will be small compared to $\Delta p_1$ and can be neglected:

$$\Delta p_{\text{sep}} \ll \Delta p_1 \tag{7.64}$$

The pressure drops through outlet 1 and the sum of the pressure drop through the membrane and outlet 2 must be equal.

$$\begin{aligned} &\Delta p_1 = \Delta p_{\text{mem}} + \Delta p_2 \\ &\Rightarrow \frac{128 \cdot \mu_1 \cdot \dot{V}_{\text{tot}}}{\pi \cdot d_1^4} L_1 = \frac{128 \cdot \mu_2 \cdot \dot{V}_2}{n \cdot \pi \cdot d_p^4} L_{\text{pore}} + \frac{128 \cdot \mu_2 \cdot \dot{V}_2}{\pi \cdot d_2^4} L_2 \end{aligned} \tag{7.65}$$

The diameter of the membrane pores and the membrane thickness are given by $d_p$ and $L_{\text{mem}}$, respectively; $n$ indicates the number of parallel pores in the membrane. Its estimation is demonstrated in Example 7.7.

To avoid the nonwetting aqueous phase penetrating the pores, the pressure drop through the membrane must be smaller than the capillary pressure:

$$\Delta p_c = \frac{4\sigma}{d_p} \cos \theta_w \tag{7.66}$$

where $\sigma$ is interfacial tension and $\theta_w$ the wetting angle.

$$\begin{aligned} &\Delta p_c > \Delta p_{\text{mem}} = \Delta p_1 - \Delta p_2 \\ &\sigma \cos \theta_w > \frac{32 \cdot \mu_2 \cdot \dot{V}_2}{n \cdot \pi \cdot d_p^3} L_{\text{pore}} \end{aligned} \tag{7.67}$$

Equation 7.67 must be respected to avoid contamination of liquid in outlet 2.

To assure that liquid will not leave through outlet 1, the flow resistance for liquid B through outlet 1 must be higher than the sum of the resistance through the membrane and outlet 2.

$$\frac{128 \cdot \mu_2 \cdot L_1}{\pi \cdot d_1^4} \gg \frac{128 \cdot \mu_2 \cdot L_{\text{pore}}}{n \cdot \pi \cdot d_p^4} + \frac{128 \cdot \mu_2 \cdot L_2}{\pi \cdot d_2^4}$$

$$\Rightarrow \frac{L_1}{d_1^4} \gg \frac{L_{pore}}{n \cdot d_p^4} + \frac{L_2}{d_2^4}$$

$$\text{with } \frac{\Delta p}{\dot{V}} = \frac{128 \cdot \mu \cdot L}{\pi \cdot d^4} : \text{the fluidic resistance} \tag{7.68}$$

**Example 7.7: Design of membrane liquid-liquid separator**

A two-phase liquid–liquid mixture is to be separated using a wettability based membrane separator with pore size ($d_p = 10\,\mu\text{m}$). Estimate the capillary pressure considering that the dispersed phase A forms a contact angle of 101° (nonwetting liquid) with the membrane material. Also, estimate the number of pores (n) required for the membrane with a length of 20 mm and a width of 1 mm. The thickness of the membrane, corresponding to the length of the pores is $\delta_{\text{mem}} = L_{\text{pore}} = 150\,\mu\text{m}$. The lengths of the outlets are 50 mm on each side. The dispersed phase outlet 1 has a diameter 0.2 mm while the continuous side outlet 2 has diameter 0.4 mm. The total liquid flow is $\dot{V}_{\text{tot}} = 1 \cdot 10^{-8}\,\text{m}^3\,\text{s}^{-1}$ with $\dot{V}_1 = \dot{V}_2$.

**Data:**

- liquid B (toluene) $\rho_{\text{toluene}} = \rho_2 = 867\,\text{kg}\,\text{m}^{-3}$, $\mu_{\text{toluene}} = \mu_2 = 0.6 \cdot 10^{-3}\,\text{Pa}\,\text{s}$,
- liquid A (water) $\rho_{\text{water}} = \rho_1 = 998.2\,\text{kg}\,\text{m}^{-3}$ $\mu_{\text{water}} = \mu_1 = 1 \cdot 10^{-3}\,\text{Pa}\,\text{s}$, $\sigma = 0.036\,\text{N}\,\text{m}^{-1}$.

***Solution:***

The dispersed aqueous phase forms a contact angle of 101° with the membrane material. The capillary pressure is given by Equation 7.66 as

$$\Delta p_c = \frac{4\sigma}{d_p} \cos\theta_w = \frac{2 \cdot 0.036}{5 \cdot 10^{-6}} |\cos(101)| = 2747.5\,\text{Pa}$$

The outlet of the aqueous phase is 50 mm long. The maximum pressure drop in outlet 1 with $\dot{V}_1 = \dot{V}_{\text{tot}}$ using Hagen–Poiseuille equation:

$$\Delta p_1 = 128 \frac{\mu_1 \cdot \dot{V} \cdot L_1}{\pi \cdot d_1^4} = 128 \cdot \frac{1 \cdot 10^{-3} (1 \cdot 10^{-8}) \cdot 50 \cdot 10^{-3}}{\pi \cdot (0.2 \cdot 10^{-3})^4} = 12.73\,\text{kPa}$$

The outlet 2 has 0.4 mm ID and 50 mm length. The pressure drop is:

$$\Delta p_2 = 128 \cdot \frac{0.6 \cdot 10^{-3} \cdot (0.5 \cdot 10^{-8}) \cdot 50 \cdot 10^{-3}}{\pi \cdot (0.4 \cdot 10^{-3})^4} = 0.24\,\text{kPa}$$

Thus, from Equation 7.65, the maximum pressure drop through the membrane is

$$\Delta p_{\text{mem}} = \Delta p_1 - \Delta p_2$$
$$= 12.73 - 0.24 = 12.5\,\text{kPa} = 128\frac{\mu_2 \dot{V}_2 L_{\text{pore}}}{n\pi d_p^4}$$

To assure that the organic liquid will not leave through outlet 1 and contaminate the aqueous flow, the flow resistance for liquid B through outlet 1 must be higher than the sum of the resistance through the membrane and outlet 2 (Equation 7.68). To satisfy Equation 7.68 we require a factor 10 times higher flow friction in outlet 1, compared to the flow friction in the membrane and outlet 2.

$$\frac{L_1}{d_1^4} = 10\left(\frac{L_{\text{pore}}}{n \cdot d_p^4} + \frac{L_2}{d_2^4}\right)$$
$$\Rightarrow n \geq \frac{10L_{\text{pore}}/d_p^4}{L_1/d_1^4 - 10 \cdot L_2/d_1^4} \cong 12800$$

### 7.6.3
### Conventional Separator Adapted for Microstructured Devices

Often microstructured reactors are used for high flow velocities where the inertial forces dominate the surface forces. In this case, a separation principle identical to conventional equipment is used. The gravity based separation, based on the density difference between two phases, is the most commonly used method of separation.

The most commonly used separator is IMM settler (see Figure 7.22) [74]. It consists of a glass tube, attached with special fittings on both ends. The biphasic mixer settles in the horizontal tube with the lighter liquid on the top and the denser liquid at the bottom. The level in a settler is adjusted by a flexible tube siphon. These settlers can be used in series for further purification of one of the liquids. This settler tested successfully for flow rates of up to 150 ml $\text{min}^{-1}$.

## 7.7
## Fluid–Fluid Reactions in Microstructured Devices

General aspects of fluid–fluid reactions are discussed in detail in Section 2.4 within the context of homogeneous catalytic reactions in biphasic systems. Mostly, the reaction takes place only in one phase and the reactant must be transferred from the nonreactant phase, for example, the gas phase to the reaction phase. In consequence, the mass transfer between the different phases plays an important role on the overall kinetics and may strongly influence the

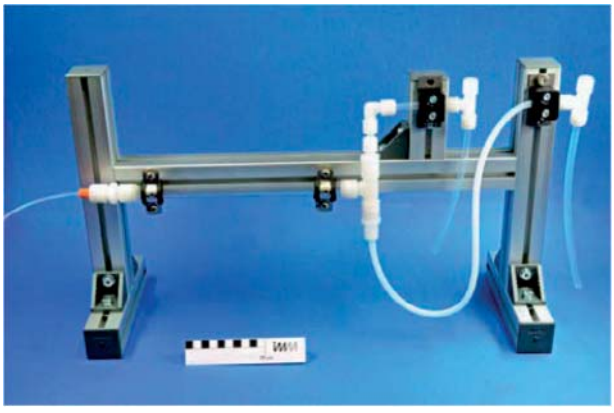

**Figure 7.22** IMM settler for separation of liquid–liquid systems [74] (Courtesy Fraunhofer ICT-IMM, Germany).

transformation rate. The influence of mass transfer on the overall reaction rate is characterized by the ratio between the characteristic mass transfer time $t_m$ and the characteristic reaction time $t_r$. This ratio is known as the *Hatta number* (*Ha*). On the basis of the film model and by supposing a pseudo first reaction in the reaction phase we obtain:

$$Ha = \sqrt{\frac{t_D}{t_r}} = \frac{\sqrt{k' D_{1,II}}}{k_L} \tag{7.69}$$

with $k'$, the rate constant of the pseudo first reaction, $D_{1,\,II}$, the molecular diffusion coefficient of reactant $A_1$ in the reaction phase (phase II), and $k_L$ the mass transfer coefficient in the reaction phase.

Depending on the value of *Ha,* different situations can be distinguished (see Figure 2.12): For $Ha \leq 0.3$ the reaction rate is slow compared to the mass transfer and the reaction takes place in the bulk phase. For values of the Hatta number $Ha > 3$, the reaction rate is very fast compared to the mass transfer rate and the reaction takes place only in the fluid film of the reaction phase near the interfacial area. Under these conditions, the transformation increases proportionally with the specific interfacial area between the phases ($a$) and the square root of the reaction rate constant (Equation 2.93):

$$r_{\text{eff}} = k_L\, a\, Ha\, c^*_{1,II} = a \cdot c^*_{1,II} \sqrt{k' \cdot D_{1,II}};$$
$$\text{with } c^*_{1,II} : \text{ equilibrium concentration at the interphase.} \tag{7.70}$$

Therefore, high transformation rates can be obtained in fluid–fluid devices with high interfacial area. Microstructured multiphase reactors are characterized by interfacial areas, which are at least 1 order of magnitude higher compared to conventional contactors, and, therefore, suited particularly for very fast reactions.

A further advantage for exothermic reactions is the generally high heat transfer performance of microstrutured reactors.

### 7.7.1 Examples of Gas–Liquid Reactions

Especially fast reactions benefit from the excellent mass transfer characteristics of microstructured devices. In addition, heat management for highly exothermic reactions is greatly facilitated because of efficient removal of heat produced during the reaction. Selective examples of different gas–liquid reactions that have been studied in the microstructured reactors are listed in Table 7.14.

#### 7.7.1.1 Halogenation

Fluorination has been carried out using conventional reactors as a multistep process, for example, the Schiemann reaction [75]. Microstructured devices have been employed for this type of reactions as direct fluorination can reduce significantly the number of steps in the synthesis of fluorinated compounds. The first application of microchannels for selective fluorination was demonstrated using the annular flow regime in order to form a film of liquid over a solid material [83]. Further, direct fluorination of toluene, pure, or dissolved in either acetonitrile or methanol was carried out using elemental fluorine [75]. Two types of reactors were employed: microstructured falling film reactor and a micro bubble column (Figure 7.23). The microstructured falling film reactor was oriented vertically and a thin liquid film was fed through orifices into the reaction channels (with $100 \times 300\,\mu m$ cross section) generating a relatively large surface for contact with the gas. In the micro bubble column the liquid and

**Table 7.14** Examples of gas–liquid reactions carried out in the microstructured reactors.

| Reaction | Reactor |
|---|---|
| Direct fluorination of toluene and nitrotoluene [75] | Microstructured falling film and micro bubble column reactor |
| Selective fluorination of 4-nitrotoluene, 1,3-dicarbonyl, and heterocyclic compounds [76] | Single micro channel operating in annular flow regime |
| Chlorination of acetic acid [77] | Microstructured falling film reactor |
| Photochlorination of toluene-2,4-diisocyanate (TDI) [78] | Microstructured falling film reactor |
| Nitration of naphthalene using $N_2O_5$ [79] | Interdigital mixers and micromixer with the split-recombine technique |
| Oxidation of alcohols and Baeyer–Villinger oxidation of ketones using elemental fluorine [80] | Single microchannel operating in annular flow regime |
| Sulfonation of toluene with gaseous sulfur trioxide [81] | Microstructured falling film reactor |
| Asymmetric hydrogenation of Z-methylacetamidocinnamate (mac) with rhodium chiral diphosphine complexes [82] | Mesh microreactor |

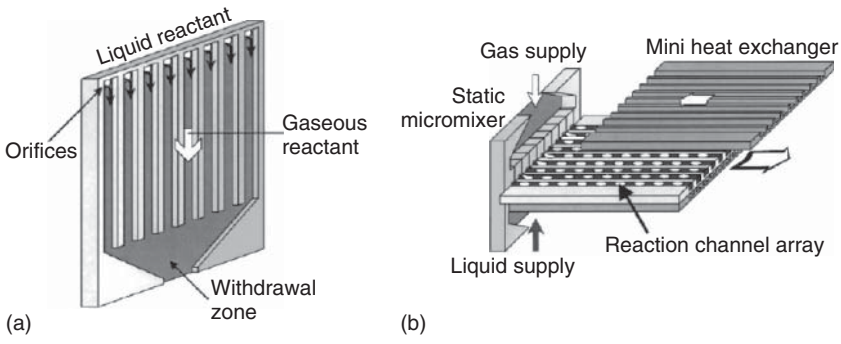


**Figure 7.23** Schematic presentation of (a) microstructured falling film reactor and (b) micro bubble column (b) [75]. (Adapted with permission from Elsevier.)

gaseous reactants are contacted through a static micromixer, and, subsequently, fed into the reaction channels. For the reaction, two types of channels, narrow ($50 \times 50\,\mu m$) and wide ($300 \times 100\,\mu m$), were used. The specific interfacial areas achieved in these channels were about $27\,000\,m^2\,m^{-3}$ for the falling film (10 μm film thickness) and about 9800 and $14\,800\,m^2\,m^{-3}$ for the micro bubble column reactors.

The microstructured falling film reactor has also been used for chlorination reactions [77]. Chlorination of acetic acid at a temperature over 140 °C was carried out and the by-product (dichloroacetic acid) was reduced significantly, meaning that there is no need for additional costly and time-consuming separation processes. Further, a photochemical gas–liquid reaction by the selective photochlorination of toluene-2,4-diisocyanate (TDI) was demonstrated [78].

#### 7.7.1.2 Nitration, Oxidations, Sulfonation, and Hydrogenation

Considering the corrosivity of nitrating agents and the explosive potential of nitro-products, microstructured devices are more suitable for such reactions compared to conventional reactors. Antes *et al.* [79] carried out the nitration of naphthalene using $N_2O_5$ as a nitrating agent. For intense contacting of the two fluids, interdigital mixers as well as microstructures with the split-recombine technique were applied. Nitration in conventional batch operation requires low temperatures to avoid thermal explosion; in microreactors the nitration was carried out at a temperature up to 50 °C and eightfold excess of $N_2O_5$ with high selectivity for mononitro naphthalene without any risk of reaction runaway.

A two-phase capillary reactor was used for the oxidation of aromatic alcohols and Baeyer–Villiger oxidation of ketones using elemental fluorine [80]. The substrate in an appropriate solvent (acetonitrile or formic acid) was injected at a controlled rate by a syringe pump into the reaction channel. Compared to batchwise operation the yield and conversion was comparable or better using microstructured devices.

The sulfonation of toluene is one of the complex reactions compared to other elemental reactions as numerous side and consecutive reactions are possible [3].

Sulfonation of toluene with gaseous $SO_3$ was carried out and very encouraging results observed [81]. With increasing $SO_3$/toluene mole ratio, the selectivity of the undesired by-products decreases while the selectivity of sulfonic acid stays nearly constant.

A well-known gas–liquid asymmetric hydrogenation of Z-methylacetamidocinnamate with rhodium chiral diphosphine complexes was carried out using a mesh microreactor [82]. The reactor has two 100 µm deep cavities (100 µl) separated by a micromesh in which the upper cavity is fed with the reacting gas while the other, the reacting chamber, contains the reacting liquid. Porosity of the mesh is 20–25%, which leads to a gas–liquid interfacial area of ~2000 $m^2\ m^{-3}$ of liquid. Mesh MSR tests can be applied to very active catalysts such as the Rh/diop complex by operation in the continuous flow mode enabling short residence times of about 1 min. If longer residence times are required, the mesh microreactor can be operated batchwise by interrupting the liquid flow using appropriate valves.

### 7.7.2 Examples of Liquid–Liquid Reactions

#### 7.7.2.1 Nitration Reaction

*Nitration of benzene* is one of the most widely used reactions for benchmarking chemical reactors for liquid–liquid application. This reaction is fast and highly exothermic (−145 kJ $mol^{-1}$). In consequence, the reactor performance is strongly influenced by mass and heat transfer. The reaction is catalyzed by sulfuric acid that creates nitrating ions ($NO_2^+$) from $HNO_3$ [69]. All reactions are assumed to take place within the acid phase. Poor mixing in this process reduces the transfer rates and leads to a buildup of dissolved nitrated products near the interface, which can be further nitrated to form often unwanted dinitro and trinitro compounds [84].

The reaction was carried out in a simple experimental microreactor setup [69]. Narrow bore capillary tubes with various lengths (50–180 cm), diameters (127–254 µm), and materials (316 stainless steel and PTFE) were used. Both phases containing reactants, acid and organic, were introduced through a T-connector to which the capillary tube was attached downstream. The tube was coiled within a controlled temperature bath. The experiments were carried out at 63–85% for $H_2SO_4$, 2.6–4.9% for $HNO_3$, 2–20 cm $s^{-1}$ flow velocities and 60–90 °C temperature. The small reactor showed higher organic transformation rates than the conventional reactor. The reaction rate was improved for higher flow velocities with high $H_2SO_4$ concentration where the production rate should depend on the mass transfer performance because of improved mixing.

*Nitration of toluene* is another exothermic nitration performed in 150 µm bore PTFE tube for varying acid strengths, reactor temperatures, and flow ratios [84]. Here too a strong influence of flow velocity on transformation rates of toluene nitration was observed:

Results from both benzene and toluene nitration have indicated that reaction rate constants in the range of 0.5–20 $min^{-1}$ can be achieved in a capillary reactor

with significant reduction in by-products formation compared to conventional processes. This may be because of isothermal environment and fundamental differences in contacting the two phases.

#### 7.7.2.2 Transesterification: Biodiesel Production

Biodiesel is a mixture of esters of high molecular fatty acids and aliphatic alcohols produced by alcoholysis of biological feedstocks with a high content of triacylglycerols. The triacylglycerol reacts stepwise with the alcohol, mostly methanol, or ethanol, to form finally the corresponding fatty acid esters and glycerol. The reaction is catalyzed by strong bases like KOH or NaOH. Initially, a biphasic mixture of triacylglycerol and alcohol is obtained. As a consequence, the first phase of the transformation is strongly influenced by mass transfer, and intensive mixing greatly accelerates the transesterification rate.

Schwarz *et al.* [85] studied the efficiency of different microstructured mixers followed by microchannels and their influence on the space time for obtaining high product yields. With increasing mass transfer performance of the micromixer and decreasing channel diameter of the microchannel reactors, shorter reaction times of several minutes at lower reaction temperatures compared to conventional batch reactor were obtained. Similar observations are reported for the synthesis of biodiesel in capillary microreactors [86] and in zigzag microchannels [87].

#### 7.7.2.3 Vitamin Precursor Synthesis

Cyclization of pseudoionone to β-ionone is an important reaction used in the synthesis of vitamin A. Conventionally, pseudoionone is slowly dosed to a stirred tank reactor containing a biphasic mixture of concentrated sulfuric acid and an organic solvent to control the temperature of the highly exothermic reaction [88]. The reaction takes place in the acid phase, where by-products are formed very quickly. The by-product formation is observed to increase with increasing temperature. The product yield obtained in conventional semibatch reactors is in the range of 70%.

Important issues in this reaction are short residence time, isothermal reaction, and defined reaction time. This can be achieved by fast mixing of the two viscous phases, the instantaneous quenching of the reaction by dilution with water after the reaction, and rapid separation of biphasic mixture.

A suitable microreactor system corresponding to the above mentioned requirements was developed by Wörz *et al.* [89]. Their installation consisted of 32 stainless steel channels of $900 \times 60\,\mu m$ size separated by cooling channels (Figure 7.24). Reactant and the acid were mixed extremely fast in these microchannels and cooled simultaneously. As the product is sensitive for consecutive reactions, it is obvious that the absence of backmixing increases the product yield. At a temperature of 20 °C, a maximum yield of 90–95% could be achieved with a residence time of 30 s. The reaction is quenched by diluting the concentrated sulfuric acid-reactant mixture with water. The dilution of concentrated sulfuric acid has an even higher exothermicity and must carried

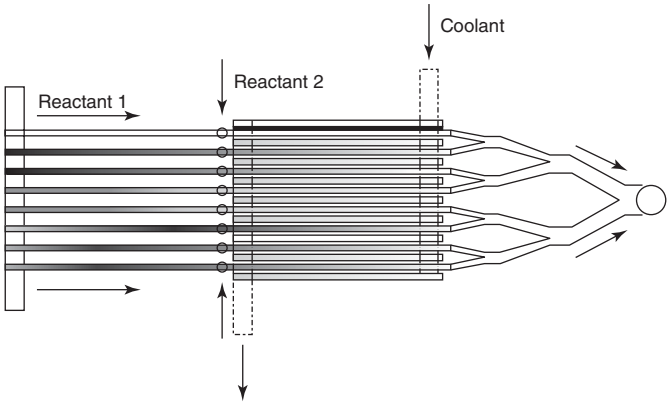


**Figure 7.24** Reactor sketch for fast, highly exothermic reactions [89]. (Adapted with permission from Elsevier.)

out in a micromixer that is embedded in an additional cooling layer. Careful construction of the microreactors is required for such application because of the danger of blockage following high viscosity and the eventual formation of polymeric products.

#### 7.7.2.4 **Phase Transfer Catalysis (PTC)**

PTC is a common approach used to accelerate a biphasic reaction by ensuring a ready supply of necessary reagent to the phase in which the reaction occurs [90, 91]. Each reactant is dissolved in the appropriate solvent, which may be immiscible and then a phase transfer catalyst is added to promote the transport of one reactant into the other phase.

*Hydrolysis of p-nitrophenyl acetate* to *p*-nitrophenyl acetate 2 was carried out in PTFE tubing (300 µm diameter, 400 mm length) using segmented flow conditions (organic phase: toluene) [92]. A phase transfer catalyst, 10 mol% tetrabutylammonium hydrogen sulfate ($Bu_4NHSO_4$), was used at 20 °C under segmented conditions. With PTC, increased reaction rate was observed compared to the case of slug flow without phase transfer catalyst. Further, sono-chemical technique was applied in which the microchannel tubing was immersed in the ultrasound bath during the reaction time. During sonication, some irregular-sized segments (1–10 µm length) were formed together with some emulsion, which increased the interfacial area. The highest reaction rates were observed when combining segmented flow, phase transfer catalyst, and sonication.

Another reaction, *alkylation reactions of β-keto esters*, is an important carbon–carbon bond-forming reactions in organic synthesis. An example is the benzylation of ethyl 2-oxocyclopentanecarboxylate (1) with benzyl bromide (2) in the presence of 5 mol% of tetrabutylammoniun bromide (TBAB) as a phase transfer catalyst as shown in Figure 7.25 [93].

The reaction was carried out in a setup depicted in Figure 7.26. The performance of the microchannel is compared to those obtained with round bottom flask for

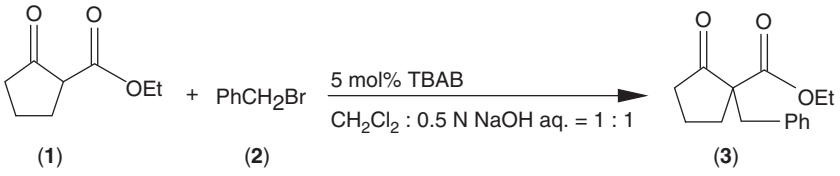


**Figure 7.25** The phase transfer benzylation reaction of ethyl 2-oxocyclopentanecarboxylate (1) with benzyl bromide (2).

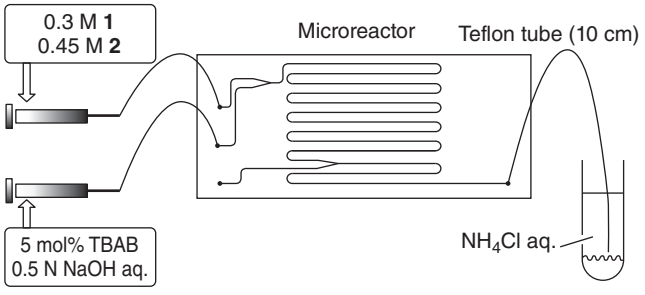


**Figure 7.26** Benzylation reaction. MSR used (channel: 200 μm width, 100 μm depth, and 45 cm length and Teflon tube: diameter 200 μm, length 10 cm). (Adapted from Ref. [93]. With permission of The Royal Society of Chemistry.)

different stirrer speed as presented in Figure 7.27. In the microchannel, the reaction proceeded smoothly, and the desired alkylation product (3) was obtained in 57% yield at 60 s, which was increased to over 90% after 300 s. A much lower yield was obtained using standard batch systems even with vigorous stirring. The result confirms the high mass transfer performance in microchannels, which are not achieved in classical batch equipment.

#### 7.7.2.5 **Enzymatic Reactions**

The enzymatic dehalogenation of *p*-chlorophenol was studied by Maruyama *et al.* [94] in a microchannel device with two-phase liquid–liquid flow. The microchannel (100 μm width, 25 μm depth) were fabricated on a glass plate (70 × 38 mm). The enzyme (laccase) was solubilized in a succinic aqueous buffer and the substrate (*p*-chlorophenol) was dissolved in isooctane. The surface of the microchannel was partially modified with octadecylsilane groups to make it hydrophobic, which allows a stable parallel flow of the aqueous and organic phases. The degradation of *p*-chlorophenol occurs only in the enzyme containing aqueous phase or at the aqueous–organic interface. At the reactor outlet a perfect phase separation could be obtained allowing the recycling of the enzyme catalyst (Figure 7.28).

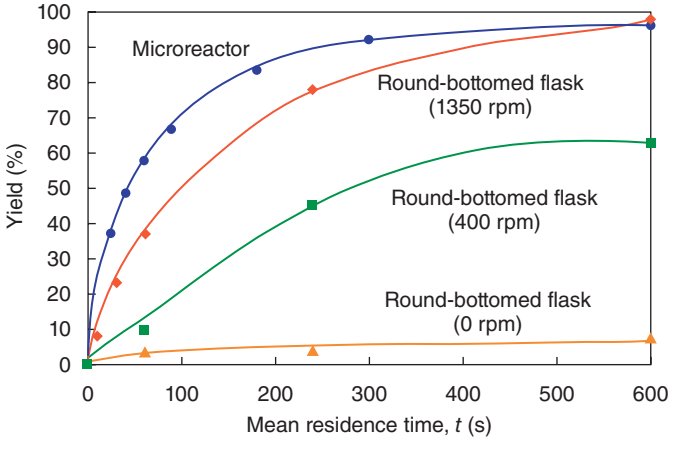


**Figure 7.27** Profile of product yield in a microreactor and standard batch systems with different mixing intensity. (Adapted from Ref. [93]. With permission of The Royal Society of Chemistry.)

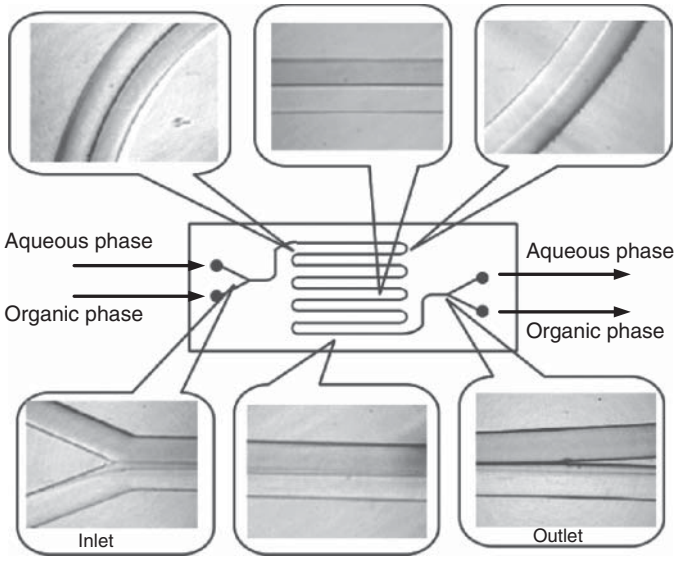


**Figure 7.28** Photographs of the parallel two-phase flow in the microchannel reactor. (Adapted from Ref. [94]. With permission of The Royal Society of Chemistry.)

## 7.8 Summary

In this chapter, different aspects of fluid–fluid systems in microstructured devices have been described. The disadvantages of conventional reactors have been clearly

mentioned and the corresponding microreactor types and their advantages have been highlighted.

Different flow regimes and corresponding mass transfer characteristics are discussed with a focus mainly on slug and parallel flow. The main parameters controlling the flow pattern are the microreactor geometry, fluid viscosity, and interfacial tension. Mass transfer performance can be interrelated using penetration model to a certain extent. The mass transfer coefficient data and correlations provided could help in the designing of microchannel reactors. These reactors are suitable for reactions with fast intrinsic kinetics, requiring high mass and heat transport leading to ameliorated reactor safety.

## 7.9 List of symbols

| | | |
|---|---|---|
| $c_{\text{int}}$ | Interfacial concentration | mol m$^{-3}$ |
| $c_m$ | Mixed-cup solute concentration | mol m$^{-3}$ |
| $c^*$ | Equilibrium concentration | mol m$^{-3}$ |
| $C'$ | Contamination in flow separation | — |
| $c^{\text{in}}$, $c^{\text{out}}$ | Concentration at inlet and outlet | mol m$^{-3}$ |
| $Ca_{L,\,u}$ | Capillary number based on two phase velocity ($u$) | — |
| $d_b$ | Diameter of dispersed slug | m |
| $f_L$, $f_{\text{tot}}$ | Liquid friction factor, two phase friction factor | — |
| $H$ | Henry's constant | Pa m$^3$ mol$^{-1}$ |
| $L_b$ | Length of dispersed slug | m |
| $l_c$ | Average distance traveled by the liquid packets along the bubble surface of the cap | m |
| $L_{\text{cir}}$ | Circumference of the channel | m |
| $L_{\text{pore}}$ | Length of the pores | m |
| $L_{\text{slug}}$ | Length of continuous (liquid) slug | m |
| $L_{\text{UC}}$ | Length of unit slug (pair of gas–liquid or liquid–liquid slugs) | |
| $n$ | Number of microchannels | — |
| $R_{\text{slip}}$ | Slip ratio between bubble and liquid velocity | — |
| $Re_D$ | Dispersed phase Reynolds number | — |
| $S$ | Flow ratio | — |
| $t_{D,\,\text{film}}$ | Diffusion time of solute in the film | s |
| $u_g$ | Gravity equivalent liquid velocity | m s$^{-1}$ |
| $u_{\text{tot}}$ | Total mixture velocity | m s$^{-1}$ |
| $V_{\text{UC}}$ | Volume of unit cell | m$^3$ |
| $\dot{V}_D$, $\dot{V}_C$ | Volumetric flow rate of dispersed, of continuous phase | m$^3$ s$^{-1}$ |
| $x_i$ | Mass fraction of phase i | — |
| $\delta_{\text{film}}$ | Thickness of wall film | m |
| $\delta_{\text{int}}$ | Thickness of hypothetical stagnant film at the interface | m |
| $\delta_{\text{mem}}$ | Thickness of the membrane | |
| $\varepsilon_C$, $\varepsilon_D$, $\varepsilon_G$, $\varepsilon_L$ | Volume fraction of continuous phase, dispersed phase, of gas, of liquid phase | — |

| | | |
|---|---|---|
| $\theta$ | Inclination angle from horizontal in falling film reactor | ° |
| $\theta_c$ | Exposure time of solute at the interface | s |
| $\theta_{c,\mathrm{cap}}$ | Average contact time of the liquid with the bubble cap | s |
| $\theta_{c,\mathrm{film}}$ | Average contact time of the liquid with the film | s |
| $\theta_w$ | Wall wetting angle | ° |
| $\varphi_D$, $\varphi_C$ | Volumetric flow fraction of dispersed phase, of continuous phase | — |
| $\tau_G$, $\tau_L$ | Residence time of gas, of liquid phase | s |
| $\Phi_G^2$, $\Phi_L^2$ | Friction multipliers for gas and liquid in Lockhart and Martinelli equation | — |
| $\Psi$ | Lockhart–Martinelli parameter | — |
| $\left(\frac{\Delta p_f}{L}\right)_L$, $\left(\frac{\Delta p_f}{L}\right)_G$ | Frictional pressure gradients when liquid and gas are assumed to flow alone | Pa m$^{-1}$ |
| $\Delta p_\mathrm{f}$ | Pressure drop due to frictional effects | Pa |
| $\left(\frac{\Delta p}{L}\right)_{\mathrm{film}}$, $\left(\frac{\Delta p}{L}\right)_{CP}$ | Pressure gradient in the slug region, single phase pressure gradient of the continuous phase | Pa m$^{-1}$ |
| $\Delta p_\mathrm{c}$ | Pressure drop due to capillary phenomena | Pa |
| $\Delta p_\mathrm{out}$ | Pressure drop in the outlets of the separator | Pa |
| $\Delta p_\mathrm{sep}$ | Pressure drop in the straight channel of separator | Pa |
| $\Delta p_\mathrm{mem}$ | Pressure drop across the membrane | Pa |

## References


1. Kashid, M.N. and Kiwi-Minsker, L. (2009) Microstructured reactors for multiphase reactions: state of the art. *Ind. Eng. Chem. Res.*, **48** (14), 6465–6485.
2. Thompson, J.C. and He, B.B. (2007) Biodiesel production using static mixers. *Trans. ASABE*, **50** (1), 161–165.
3. Hessel, V., Angeli, P., Gavriilidis, A., and Löwe, H. (2005) Gas-liquid and gas-liquid-solid microstructured reactors: contacting principles and applications. *Ind. Eng. Chem. Res.*, **44** (25), 9750–9769.
4. Benz, K., Jäckel, K.P., Regenauer, K.J., Schiewe, J., Drese, K., W.E., Hessel, V., and Löwe, H. (2001) Utilization of micromixers for extraction processes. *Chem. Eng. Technol.*, **24** (1), 11–17.
5. Ehrfeld, W., Hessel, V., and Löwe, H. (2000) *Microreactors*, Wiley-VCH Verlag GmbH, Weinheim.
6. Jähnisch, K., Hessel, V., Löwe, H., and Baerns, M. (2004) Chemistry in microstructured reactors. *Angew. Chem. Int. Ed.*, **43** (4), 406–446.
7. Robins, I., Shaw, J., Miller, B., Turner, C., and Harper, M. (1997) *Microreaction Technology, 1st International Conference on Microreaction Technology*, Springer-Verlag, Berlin, pp. 35–46.
8. Shaw, J., Turner, C., Miller, B., Robins, I., Kingston, I., and Harper, M. (1998) Characterization of micro-contactors for solute transfer between immiscible liquid and development of arrays for high throughput. 2nd International Conference on Microreaction Technology, Topical Conference Preprints, AIChE, New Orleans, LA.
9. TeGrotenhuis, W.E., Cameron, R.J., Butcher, M.G., Martin, P.M., and Wegeng, R.S. (1998) Microchannel devices for efficient contacting of liquids in solvent extraction. Process Miniaturization: 2nd International Conference on

Microreaction Technology, 1998, AIChE, New Orleans, LA, pp. 329–334.
10. TeGrotenhuis, W.E., Cameron, R.J., Viswanathan, V.V., and Wegeng, R.S. (2000) *Microreactor Technology: 3rd International Conference on Microreaction Technology; Topical Conference Preprints*, Springer-Verlag, Berlin, pp. 541–549.
11. Ehrfeld, W., Gärtner, C., Golbig, K., Hessel, V., Konrad, R., Löwe, H., Richter, T., and Schulz, C. (1997) *Microreactor Technology: 1st International Conference on Microreactor Technology*, Springer-Verlag, Berlin, pp. 72–90.
12. Köhler, J.M., Henkel, T., Grodrian, A., Kirner, T., Roth, M., Martin, K., and Metze, J. (2004) Digital reaction technology by micro segmented flow – components, concepts and applications. *Chem. Eng. J.*, **101** (1-3), 201–216.
13. Jadhavrao, P. (2007) *Suzuki Coupling Based Polycondensation Using Enhanced Dispersing in High-p, T Micro Process Technology Devices*, Technical University of Dortmund, Dortmund.
14. De Bellefon, C., Lamouille, T., Pestre, N., Bornette, F., Pennemann, H., Neumann, F., and Hessel, V. (2005) Asymmetric catalytic hydrogenations at micro-litre scale in a helicoidal single channel falling film micro-reactor. *Catal. Today*, **110** (1-2), 179–187.
15. Hassan, I., Vaillancourt, M., and Pehlivan, K. (2005) Two-phase flow regime transitions in microchannels: a comparative experimental study. *Microscale Thermophys. Eng.*, **9** (2), 165–182.
16. Liu, H., Vandu, C.O., and Krishna, R. (2005) Hydrodynamics of Taylor flow in vertical capillaries: flow regimes, bubble rise velocity, liquid slug length, and pressure drop. *Ind. Eng. Chem. Res.*, **44** (14), 4884–4897.
17. Shao, N., Gavriilidis, A., and Angeli, P. (2009) Flow regimes for adiabatic gas-liquid flow in microchannels. *Chem. Eng. Sci.*, **64** (11), 2749–2761.
18. Gañán-Calvo, A.M. and Gordillo, J.M. (2001) Perfectly monodisperse microbubbling by capillary flow focusing. *Phys. Rev. Lett.*, **87** (27 I), 2745011–2745014.
19. Gavriilidis, A. and Angeli, P. (2009) Mixing and contacting of heterogeneous systems, in *Handbook of Micro Reactors: Fundamentals, Operations and Catalysts* (eds V. Hessel, J.C. Schouten, A. Renken, and J.-I. Yoshida), Wiley-VCH Verlag GmbH & Co. KGaA, Weinheim.
20. Cubaud, T., Tatineni, M., Zhong, X., and Ho, C.M. (2005) Bubble dispenser in microfluidic devices. *Phys. Rev. E Stat. Nonlinear Soft Matter Phys.*, **72** (3), 1–4.
21. Whitesides, G.M. (2006) The origins and the future of microfluidics. *Nature*, **442** (7101), 368–373.
22. Löb, P., Pennemann, H., and Hessel, V. (2004) g/l-Dispersion in interdigital micromixers with different mixing chamber geometries. *Chem. Eng. J.*, **101** (1-3), 75–85.
23. Yasuno, M., Sugiura, S., Iwamoto, S., Nakajima, M., Shono, A., and Satoh, K. (2004) Monodispersed microbubble formation using microchannel technique. *AIChE J.*, **50** (12), 3227–3233.
24. Pennemann, H., Hessel, V., Kost, H.J., Löwe, H., and De Bellefon, C. (2004) Investigations on pulse broadening for catalyst screening in gas/liquid systems. *AIChE J.*, **50** (8), 1814–1823.
25. Kashid, M.N., Renken, A., and Kiwi-Minsker, L. (2010) CFD modelling of liquid-liquid multiphase microstructured reactor: slug flow generation. *Chem. Eng. Res. Des.*, **88** (3), 362–368.
26. Berčič, G. and Pintar, A. (1997) The role of gas bubbles and liquid slug lengths on mass transport in the Taylor flow through capillaries. *Chem. Eng. Sci.*, **52** (21-22), 3709–3719.
27. Günther, A., Khan, S.A., Thalmann, M., Trachsel, F., and Jensen, K.F. (2004) Transport and reaction in microscale segmented gas-liquid flow. *Lab Chip - Miniaturisation Chem. Biol.*, **4** (4), 278–286.
28. Bretherton, F.P. (1961) The motion of long bubbles in tubes. *J. Fluid Mech.*, **10** (2), 166–188.
29. Aussillous, P. and Quere, D. (2000) Quick deposition of a fluid on the wall of a tube. *Phys. Fluids*, **12** (10), 2367–2371.

30. Kreutzer, M.T. (2003) *Hydrodynamics of Taylor Flow in Capillaries and Monolith Reactors*, Delft University, Delft.
31. Chung, P.M.Y. and Kawaji, M. (2004) The effect of channel diameter on adiabatic two-phase flow characteristics in microchannels. *Int. J. Multiphase Flow*, **30** (Special Issue 7-8), 735–761.
32. Yue, J., Chen, G., Yuan, Q., Luo, L., and Gonthier, Y. (2007) Hydrodynamics and mass transfer characteristics in gas-liquid flow through a rectangular microchannel. *Chem. Eng. Sci.*, **62** (7), 2096–2108.
33. Kashid, M.N., Renken, A., and Kiwi-Minsker, L. (2011) Gas-liquid and liquid-liquid mass transfer in microstructured reactors. *Chem. Eng. Sci.*, **66** (17), 3876–3897.
34. Tice, J.D., Song, H., Lyon, A.D., and Ismagilov, R.F. (2003) Formation of droplets and mixing in multiphase microfluidics at low values of the Reynolds and the capillary numbers. *Langmuir*, **19** (22), 9127–9133.
35. Burns, J.R. and Ramshaw, C. (2001) The intensification of rapid reactions in multiphase systems using slug flow in capillaries. *Lab Chip*, **1** (1), 10–15.
36. Dessimoz, A.L., Cavin, L., Renken, A., and Kiwi-Minsker, L. (2008) Liquid-liquid two-phase flow patterns and mass transfer characteristics in rectangular glass microreactors. *Chem. Eng. Sci.*, **63** (16), 4035–4044.
37. Kashid, M.N. and Agar, D.W. (2007) Hydrodynamics of liquid-liquid slug flow capillary microreactor: flow regimes, slug size and pressure drop. *Chem. Eng. J.*, **131** (1-3), 1–13.
38. Burns, J.R. and Ramshaw, C. (1999) Development of a microreactor for chemical production. *Trans. Inst. Chem. Eng.*, **77A**, 206–211.
39. TeGrotenhuis, W.E., Cameron, R.J., Butcher, M.G., Martin, P.M., and Wegeng, R.S. (1999) Microchannel devices for efficient contacting of liquids in solvent extraction. *Sep. Sci. Technol.*, **34** (6-7), 951–974.
40. Kashid, M. and Kiwi-Minsker, L. (2011) Quantitative prediction of flow patterns in liquid-liquid flow in micro-capillaries. *Chem. Eng. Process.*, **50** (10), 972–978.
41. Whitman, W.G. (1923) Preliminary experimental confirmation of the two-film theory of gas absorption. *Chem. Metall. Eng.*, **29**, 146–148.
42. Higbie, R. (1935) The rate of absorption of a pure gas into a still liquid during short periods of exposure. *Trans. Am. Inst. Chem. Eng.*, **31**, 365–389.
43. Dobbins, W.E. (1956) in *Biological Treatment of Sewage and Industrial Wastes* (eds M.L. McCable and W.W. Eckenfelder), Reinhold, New York.
44. Toor, H.L. and Marchello, J.M. (1958) Film-penetration model for mass and heat transfer. *AIChE J.*, **4** (1), 97–101.
45. Irandoust, S., Ertle, S., and Andersson, B. (1992) Gas-liquid mass transfer in Taylor flow through a capillary. *Can. J. Chem. Eng.*, **70**, 115–119.
46. Vandu, C.O., Liu, H., and Krishna, R. (2005) Mass transfer from Taylor bubbles rising in single capillaries. *Chem. Eng. Sci.*, **60** (22), 6430–6437.
47. van Baten, J.M. and Krishna, R. (2004) CFD simulations of mass transfer from Taylor bubbles rising in circular capillaries. *Chem. Eng. Sci.*, **59** (12), 2535–2545.
48. Heiszwolf, J.J., Kreutzer, M.T., Van Den Eijnden, M.G., Kapteijn, F., and Moulijn, J.A. (2001) Gas-liquid mass transfer of aqueous Taylor flow in monoliths. *Catal. Today*, **69** (1-4), 51–55.
49. Pohorecki, R. (2007) Effectiveness of interfacial area for mass transfer in two-phase flow in microreactors. *Chem. Eng. Sci.*, **62** (22), 6495–6498.
50. Zhang, H., Chen, G., Yue, J., and Yuan, Q. (2009) Hydrodynamics and mass transfer of gas-liquid flow in a falling film microreactor. *AIChE J.*, **55** (5), 1110–1120.
51. Sobieszuk, P., Pohorecki, R., Cyganski, P., Kraut, M., and Olschewski, F. (2010) Marangoni effect in a falling film microreactor. *Chem. Eng. J.*, **164** (1), 10–15.
52. Ziegenbalg, D., Löb, P., Al-Rawashdeh, M., Kralisch, D., Hessel, V., and Schönfeld, F. (2010) Use of 'smart interfaces' to improve the liquid-sided mass transport in a falling film microreactor. *Chem. Eng. Sci.*, **65** (11), 3557–3566.

53. Cantu-Perez, A., Al-Rawashdeh, M., Hessel, V., and Gavriilidis, A. (2013) Reaction modelling of a microstructured falling film reactor incorporating staggered herringbone structures using eddy diffusivity concepts. *Chem. Eng. J.*, **227**, 34–41.
54. Kashid, M.N., Harshe, Y.M., and Agar, D.W. (2007) Liquid-liquid slug flow in a capillary: an alternative to suspended drop or film contactors. *Ind. Eng. Chem. Res.*, **46** (25), 8420–8430.
55. Kashid, M., Renken, A., and Kiwi-Minsker, L. (2011) Influence of flow regime on mass transfer in different types of microchannels. *Ind. Eng. Chem. Res.*, **50** (11), 6906–6914.
56. Zhao, Y., Chen, G., and Yuan, Q. (2007) Liquid-liquid two-phase mass transfer in the T-junction microchannels. *AIChE J.*, **53** (12), 3042–3053.
57. Fernandes, J.B. and Sharma, M.M. (1967) Effective interfacial area in agitated liquid-liquid contactors. *Chem. Eng. Sci.*, **22** (10), 1267–1282.
58. Verma, R.P. and Sharma, M.M. (1975) Mass transfer in packed liquid-liquid extraction columns. *Chem. Eng. Sci.*, **30** (3), 279–292.
59. Alper, E. (1988) Effective interfacial area in the RTL extractor from rates of extraction with chemical reaction. *Chem. Eng. Res. Des.*, **66** (2), 147–151.
60. Dehkordi, A.M. (2002) Liquid-liquid extraction with chemical reaction in a novel impinging-jets reactor. *AIChE J.*, **48** (10), 2230–2239.
61. Dehkordi, A.M. (2001) Novel type of impinging streams contactor for liquid-liquid extraction. *Ind. Eng. Chem. Res.*, **40** (2), 681–688.
62. Kockmann, N. (2008) Transport phenomena in micro process engineering, in *Heat and Mass Transfer* (eds D. Mewes and F. Mayinger), Springer-Verlag, Berlin, Heidelberg.
63. Lockhart, R.W. and Martinelli, R.C. (1949) Proposed correlation of data for isothermal 2-phase, 2-component flow in pipes. *Chem. Eng. Prog.*, **45** (1), 39–48.
64. Chisholm, D. (1967) A theoretical basis for lockhart-martinelli correlation for 2-phase flow. *Int. J. Heat Mass Transfer*, **10** (12), 1767.
65. Tilton, J.N. (1997) Fluid and particle dynamics, in *Perry's Chemical Engineers' Handbook* (eds R.H. Perry, D.W. Green, and J.O. Maloney), McGraw-Hill, New York etc.
66. Charles, M.E. (1963) The pipeline flow of capsules (Part 2). *Can. J. Chem. Eng.*, **41**, 46–51.
67. Kashid, M.N. (2007) *Experimental and Modelling Studies on Liquid-Liquid Slug Flow Capillary Microreactors*, University of Dortmund, Dortmund.
68. Kiwi-Minsker, L. and Renken, A. (2008) in *Handbook of Heterogeneous Catalysis* (eds G. Ertl, H. Knözinger, F. Schüth, and J. Weitkamp), Wiley-VCH Verlag GmbH, Weinheim, pp. 2248–2264.
69. Burns, J.R. and Ramshaw, C. (1999) Development of a microreactor for chemical production. *Chem. Eng. Res. Des.*, **77** (A3), 206–211.
70. Kashid, M., Renken, A., and Kiwi-Minsker, L. (2013) Effects of microfluidics on prparative chemistry processes, in *Microreactors in Preparative Chemistry* (ed. W. Reschetilowski), Wiley-VCH Verlag GmbH, Weinheim.
71. Yamasaki, Y., Kariyasaki, A., and Morooka, S. (2010) Hydrophilic and hydrophobic modifications of microchannel inner walls for liquid-liquid laminar layered flows. *Int. J. Chem. Reactor Eng.*, **8**, 17.
72. Kralj, J.G., Sahoo, H.R., and Jensen, K.F. (2007) Integrated continuous microfluidic liquid-liquid extraction. *Lab Chip - Miniaturization Chem. Biol.*, **7** (2), 256–263.
73. Hoettges, K.F., Stevenson, D., Homewood, K.P., and Gwilliam, R.M. (2003) Liquid-liquid separation. WO Patent 03/082429:A2, p. 46.
74. Rothstock, S., Werner, B., Hofmann, C., Schütt, C., Kost, H.-J., Löb, P., Hessel, V., and Löwe, H. (2008) Development of microstructued reactors and a following continuous work-up system for liquid/liquid reactions for use in polycondensation. 10th International Conference on Microreaction Technology, IMRET-10 2008, AIChE, New Orleans, LA, pp. 513–518.
75. Jähnisch, K., Baerns, M., Hessel, V., Ehrfeld, W., Haverkamp, V., Löwe,

H., Wille, C., and Guber, A. (2000) Direct fluorination of toluene using elemental fluorine in gas/liquid microreactors. *J. Fluorine Chem.*, **105** (1), 117–128.

76. Chambers, R.D., Rolling, D., Spink, R.C.H., and Sandford, G. (2001) Elemental fluorine part 13: gas-liquid thin film microreactors for selective direct fluorination. *Lab Chip: Miniaturization Chem. Biol.*, **1** (2), 132–137.
77. Wehle, D., Dejmek, M., Rosenthal, J., Ernst, H., Kampmann, D., Trautschold, S., and Pechatschek, R. (2000) Monochloroacetic acid production by high temperature chlorination of acetic acid with chlorine 83. WO Patent 200210094-A; DE Patent 10036603-A1; WO Patent 200210094-A1.
78. Ehrich, H., Linke, D., Morgenschweis, K., Baerns, M., and Jähnisch, K. (2002) Application of microstructured reactor technology for the photochemical chlorination of alkylaromatics. *Chimia*, **56** (11), 647–653.
79. Antes, J., Tuercke, T., Kerth, J., Marioth, E., Schnuerer, F., Krause, H.H., and Loebbecke, S. (2001) Use of microreactors for nitration processes. 4th International Conference on Microreaction Technology (IMRET 4), 2001, Atlanta, GA.
80. Chambers, R.D., Holling, D., Rees, A.J., and Sandford, G. (2003) Microreactors for oxidations using fluorine. *J. Fluorine Chem.*, **119** (1), 81–82.
81. Müller, A., Cominos, V., Hessel, V., Horn, B., Schürer, J., Ziogas, A., Jähnisch, K., Hillmann, V., Großer, V., Jam, K.A., Bazzanella, A., Rinke, G., and Kraut, M. (2005) Fluidic bus system for chemical process engineering in the laboratory and for small-scale production. *Chem. Eng. J.*, **107** (1-3), 205–214.
82. Abdallah, R., Meille, V., Shaw, J., Wenn, D., and De Bellefon, C. (2004) Gas-liquid and gas-liquid-solid catalysis in a mesh microreactor. *Chem. Commun.*, **10** (4), 372–373.
83. Chambers, R.D., Hutchinson, J., and Sandford, G. (1999) Recent studies at Durham on direct fluorination. *J. Fluorine Chem.*, **100** (1-2), 63–73.
84. Burns, J.R. and Ramshaw, C. (2002) A microreactor for the nitration of benzene and toluene. *Chem. Eng. Commun.*, **189** (12), 1611–1628.
85. Schwarz, S., Borovinskaya, E.S., and Reschetilowski, W. (2013) Base catalyzed ethanolysis of soybean oil in microreactors: experiments and kinetic modeling. *Chem. Eng. Sci.*, **104**, 610–618.
86. Sun, J., Ju, J., Ji, L., Zhang, L., and Xu, N. (2008) Synthesis of biodiesel in capillary microreactors. *Ind. Eng. Chem. Res.*, **47** (5), 1398–1403.
87. Wen, Z., Yu, X., Tu, S.T., Yan, J., and Dahlquist, E. (2009) Intensification of biodiesel synthesis using zigzag microchannel reactors. *Bioresour. Technol.*, **100** (12), 3054–3060.
88. Kashid, M.N., Yuranov, I., Raspail, P., Prechtl, P., Membrez, J., Renken, A., and Kiwi-Minsker, L. (2011) Cyclization of pseudoionone to β-Ionone: reaction mechanism and kinetics. *Ind. Eng. Chem. Res.*, **50** (13), 7920–7926.
89. Wörz, O., Jäckel, K.P., Richter, T., and Wolf, A. (2001) Microreactors, a new efficient tool for optimum reactor design. *Chem. Eng. Sci.*, **56** (3), 1029–1033.
90. Sasson, Y. and Neumann, R. (eds) (1997) *Handbook of Phase Transfer Catalysis*, Blackie Academics and Professionals, London.
91. Fiamegos, Y.C. and Stalikas, C.D. (2005) Phase-transfer catalysis in analytical chemistry. *Anal. Chim. Acta*, **550** (1-2), 1–12.
92. Ahmed-Omer, B., Barrow, D., and Wirth, T. (2007) Effect of segmented fluid flow, sonication and phase transfer catalysis on biphasic reactions in capillary microreactors. *Chem. Eng. J.*, **135** (Suppl. 1), S280–S283.
93. Ueno, M., Hisamoto, H., Kitamori, T., and Kobayashi, S. (2003) Phase-transfer alkylation reactions using microreactors. *Chem. Commun.*, **8**, 936–937.
94. Maruyama, T., Uchida, J.I., Ohkawa, T., Futami, T., Katayama, K., Nishizawa, K.I., Sotowa, K.I., Kubota, F., Kamiya, N., and Goto, M. (2003) Enzymatic degradation of p-chlorophenol in a two-phase flow microchannel system. *Lab*

*Chip - Miniaturization Chem. Biol.*, **3** (4), 308–312.

**95.** Yeong, K.K., Gavriilidis, A., Zapf, R., and Hessel, V. (2003) Catalyst preparation and deactivation issues for nitrobenzene hydrogenation in a microstructured falling film reactor. *Catal. Today*, **81** (4), 641–651.